# Hierarchies of Critical Points of a Landau-de Gennes Free Energy on Three-Dimensional Cuboids

**Baoming Shi[1], Yucen Han[2], Jianyuan Yin[3], Apala Majumdar[2] and Lei Zhang[4,\*]**

[1] School of Mathematical Sciences, Peking University, Beijing 100871, China.

[2] Department of Mathematics and Statistics, University of Strathclyde, Glasgow, G1 1XH, UK.

[3] Department of Mathematics, National University of Singapore, Singapore 119076.

[4] Beijing International Center for Mathematical Research, Center for Quantitative Biology, Peking University, Beijing 100871, China.

E-mail: ming123@stu.pku.edu.cn, yucen.han@strath.ac.uk, yinjy@nus.edu.sg, apala.majumdar@strath.ac.uk, zhangl@math.pku.edu.cn

**Abstract.** We investigate critical points of a Landau-de Gennes (LdG) free energy in three-dimensional (3D) cuboids, that model nematic equilibria. We develop a hybrid saddle dynamics-based algorithm to efficiently compute solution landscapes of these 3D systems. Our main results concern (a) the construction of 3D LdG critical points from a database of 2D LdG critical points and (b) studies of the effects of cross-section size and cuboid height on solution landscapes. In doing so, we discover multiple-layer 3D LdG critical points constructed by stacking 3D critical points on top of each other, novel pathways between distinct energy minima mediated by 3D LdG critical points and novel metastable escaped solutions, all of which can be tuned for tailor-made static and dynamic properties of confined nematic liquid crystal systems in 3D.

*Keywords*: Landau–de Gennes model, three-dimensional cuboid, nematic liquid crystals, solution landscape, saddle point, bifurcation, transition pathway

## 1. Introduction

Liquid crystals are mesophases intermediate between the solid and liquid states. The simplest liquid crystal phase is the nematic phase for which the constituent molecules have no positional order, but tend to align along certain locally preferred directions [1], referred to as *nematic directors*. Consequently nematic liquid crystals (NLCs) have direction-dependent physical, optical and rheological properties [2, 3]. Thus, NLCs have widespread applications in opto-electronics, nanodevices and materials technologies. A crucial feature of NLC systems concern topological (point or line) defects, interpreted as discontinuities in the directors, which have been visualized in polymeric materials or through mesoscale simulations of the local orientation of the molecules [4]. The defects play important roles in self-assembled structures, colloidal suspensions and multistable

*Hierarchies of Critical Points of a Landau-de Gennes Free Energy* 2

systems, and often label families of observable equilibria and transient states in static and dynamic phenomena for confined NLC systems [5, 6, 7].

There are multiple microscopic, mean-field and macroscopic/continuum theories for NLCs, e.g. Maier-Saupe, Oseen-Frank, Ericksen theories and the Landau-de Gennes (LdG) theory, which is the most powerful and general continuum theory amongst its competitors [8, 9]. The LdG theory is a variational theory and describes the NLC state by a macroscopic order parameter, the **Q**-tensor order parameter with five degrees of freedom, and the physically observable NLC states as minimizers of an appropriately defined LdG free energy, subject to physically relevant boundary conditions. Of course, the LdG free energy typically has multiple energy minimizers and non energy-minimizing critical points, all of which make the mathematics and physics of NLCs challenging and fascinating. The precise details are given in the next section, but there has been substantial recent work on the reduced LdG model, valid for two-dimensional (2D) confinement and for planar director profiles [10, 11, 12, 13]. In this reduced LdG framework, there are only two degrees of freedom and the reduced LdG energy effectively reduces to the celebrated Ginzburg-Landau energy for superconductors [14]. There has been a body of work for reduced LdG critical points on a 2D square domain with tangent boundary conditions, motivated by the experimental work in [15]. For small squares on the nano-scale, there is a unique reduced LdG critical point, coined as the Well Order Reconstruction Solution (WORS), which has a pair of orthogonal line defects along square diagonals [16]. The WORS is globally stable when the square edge length is sufficiently small, but loses stability as the edge length increases [10]. For a large square domain, there are two types of experimentally observed stable states: the diagonal (D) state for which the director is aligned along the square diagonal and the rotated (R) state for which the director rotates by $\pi$ radians between a pair of opposite square edges [15]. In [17], the authors investigate the solution landscape of the reduced LdG model on square domains, and recover the typical WORS, D, and R states, along with new unstable states that have multiple point/line defects, and the switching mechanisms between them. More generally, reduced LdG models have been studied on 2D polygons such as a hexagon, 2D discs and rectangles, and the reader is referred to [18, 19, 20, 21].

The 2D studies cited above are limiting cases of 3D studies, with vanishing height [14]. This raises the fundamentally important question - reduced 2D studies only exploit two out of five degrees of freedom in the LdG framework and how do the additional degrees of freedom manifest in 3D? From an application point of view, 3D studies are much needed in generic scenarios such as liquid crystal displays, food science, and biology [22]. In general, 2D solutions (or critical points of a reduced LdG free energy) can be viewed as $z$-invariant 3D LdG critical points, invariant in the third dimension. With an additional dimension in 3D, we have the possibility of 3D $z$-variant solutions with complicated defect structures [4, 23], more complicated solution landscapes with $z$-variant 3D stable and unstable critical points, $z$-variant pathways between different critical points and far greater tunability of solution landscapes for designer material properties. In [24], the authors report a mixed solution in a 3D cuboid that interpolates

between two distinct stable D states, on the top and bottom cuboid surfaces. In a cylinder, we have a 3D escaped solution with two ring disclinations, and the domino-like transition pathway mediated by a $z$-variant unstable LdG critical point is energetically preferable to the $z$-invariant pathways [25]. Various 3D knotted defect fields in confined NLCs are shown in [26], which cannot be captured by 2D studies alone. The authors of [4] report the experimental visualization of the defect structure, and demonstrate the continuous switching between a $+1/2$ point defect and a $-1/2$ defect by twisting along $z$-direction, again outside the remit of 2D studies. These genuinely 3D features of confined NLCs motivate us to systematically study LdG solution landscapes, with the full five degrees of freedom, on a 3D cuboid as a generic example, by using 2D critical points in [11, 17] as a solution database.

In this paper, we focus on critical points of a LdG free energy on a 3D cuboid, with the full five degrees of freedom, that model nematic equilibria and admissible nematic states, imposing tangent Dirichlet boundary conditions on lateral surfaces and natural boundary condition on top and bottom surfaces. There are two geometry-dependent variables: the edge length of the square cross-section denoted by $\lambda$, and the cuboid height denoted by $h$. Our goal is to use the database of reduced 2D LdG critical points in [11, 17] (for a square domain) to systematically construct both $z$-invariant and $z$-variant critical points of a 3D LdG energy. In doing so, we find that many $z$-variant solutions have inherently small eigenvalues for the Hessian of the LdG energy, reflected in the insignificant energy cost of moving cross-sectional solution profiles up and down, provided $h$ is large enough. We design a hybrid numerical scheme to deal with the ill conditioned saddle dynamics and convergence issues, caused by such small eigenvalues. This hybrid numerical scheme for the saddle dynamics allows us to efficiently explore the solution landscapes of this 3D system as a function of $\lambda$ and $h$, with special attention to the elusive unstable LdG critical points and how to control their instabilities. Our first numerical result concerns the 3D $z$-invariant critical points that are a translationally invariant version of the 2D reduced LdG critical points. These 2D critical points survive in 3D but are *more unstable* in 3D, i.e. they have higher Morse indices or equivalently, more unstable directions in 3D compared to 2D. Our main results concern new 3D LdG critical points, labelled as $A - B - C$, where $A$, $B$ and $C$ are reduced 2D LdG critical points, $A$ is the profile on the top cuboid surface, $B$ corresponds to the middle slice and $C$ corresponds to the bottom slice. In particular, we can use pathways, $A \to B \to C$ on the 2D solution landscape, where $B$ has a higher Morse index than $A$ and $C$, to construct such 3D LdG critical points, labelled by $A - B - C$. We believe these numerical results to be of wide interest, since they provide a general recipe (which could fail in some situations) for constructing higher-dimensional critical points of a free energy from lower-dimensional critical points. The recipe is intuitive but the plethora of numerical results, the symmetries of the 3D LdG critical points and their defect sets give great inroads into cutting-edge computational and modelling questions at the interface of theory and applications. There are some interesting by-products of these numerical experiments, which could be relevant for novel NLC applications engineered with 3D

cuboids. We explore 3D nematic solution landscapes as outlined above and in doing so, find an energetically favourable pathway between two $z$-invariant energy-minimizing D states, and this pathway is featured by a $z$-variant transition state, for large enough $\lambda$ and $h$. Thus, $z$-variant critical points can be relevant for the switching between $z$-invariant states, which is interesting in its own right.

We also numerically compute bifurcation diagrams for the 3D LdG critical points, as a function of $\lambda$ and $h$, which show that $z$-invariant solutions become more unstable while some $z$-variant solutions become more stable, as $h$ increases. We observe the emergence of multiple-layer solutions, which are effectively blocks of dual 3D LdG critical points stacked on top of each other, and the Morse indices of these multi-layered solutions depend on the number of layers. Whilst we solve for the full five degrees of freedom for the LdG $\mathbf{Q}$-tensor and allow for all variables to depend on all three spatial dimensions, the majority of our numerical results only have three degrees of freedom and the $z$-variant critical points emerge from the $z$-dependence of the degrees of freedom or the $z$-dependence of the nematic directors i.e. the nematic directors lie in the xy-plane but are not translationally invariant. In the last sub-section, we numerically find a branch of escaped solutions for which the directors are out-of-plane, and which exploit the full five degrees of freedom, including the metastable escaped central (EC) state, and we investigate the transition pathway between the EC state and energy-minimizing $z$-invariant D state.

This paper is organized as follows. In Sec. 2, we briefly review the LdG theory for NLCs and introduce the domain and the boundary conditions. In Sec. 3, we propose a hybrid numerical scheme for the saddle dynamics to speed up the computation of saddle points. In Sec. 4, we present a detailed study of the 3D LdG model on cuboid. We finally present our conclusions in Sec. 5.

## 2. The Landau–de Gennes theory

We work within the celebrated LdG theory, which is the most general continuum theory for nematic liquid crystals (NLCs). The LdG theory describes the NLC state by a macroscopic order parameter, the LdG $\mathbf{Q}$-tensor order parameter, that distinguishes NLCs from isotropic liquids in terms of anisotropic macroscopic quantities, such as the magnetic susceptibility and dielectric anisotropy [1]. Mathematically, the $\mathbf{Q}$-tensor is given by a symmetric, traceless $3 \times 3$ matrix as shown below:

$$\mathbf{Q} = \begin{pmatrix} q_1 - q_3 & q_2 & q_4 \\ q_2 & -q_1 - q_3 & q_5 \\ q_4 & q_5 & 2q_3 \end{pmatrix}. \tag{1}$$

From the spectral decomposition theorem, we can write the $\mathbf{Q}$-tensor as

$$\mathbf{Q} = \sum_{i=1}^{3} \lambda_i \mathbf{e}_i \otimes \mathbf{e}_i,$$

where $\{\mathbf{e}_1, \mathbf{e}_2, \mathbf{e}_3\}$ are the eigenvectors of the $\mathbf{Q}$-tensor and $\lambda_1 \leqslant \lambda_2 \leqslant \lambda_3$ are the associated eigenvalues respectively, subject to $\sum_{i=1}^{3} \lambda_i = 0$. The eigenvectors model the preferred directions of spatially averaged local molecular alignment in space or the nematic directors, and the eigenvalues are a measure of the degree of orientational order about these directions. A $\mathbf{Q}$-tensor is said to be isotropic if $\mathbf{Q} = \mathbf{0}$, uniaxial if $\mathbf{Q}$ has a pair of repeated non-zero eigenvalues, and biaxial if $\mathbf{Q}$ has three distinct eigenvalues [1, 27]. Physically, a uniaxial NLC phase has a single distinguished direction of averaged molecular alignment, such that all directions perpendicular to the uniaxial director are physically equivalent. A biaxial phase has a primary and secondary nematic director.

The LdG theory is a variational theory, based on the premise that the physically observable configurations are modelled by minimizers of an appropriately defined LdG free energy [1]. There are several forms of the LdG free energy, and in this manuscript we work with a particularly simple form:

$$E[\mathbf{Q}] := \int_V \left[ \frac{L}{2} |\nabla \mathbf{Q}|^2 + f_B(\mathbf{Q}) \right] \mathrm{d}A, \tag{2}$$

where the first term in the integrand is the Dirichlet elastic energy density that penalizes spatial inhomogeneities, and the second term is the thermotropic potential, $f_B$ that dictates the preferred NLC phase as a function of temperature.

$$|\nabla \mathbf{Q}|^2 := \frac{\partial Q_{ij}}{\partial r_k} \frac{\partial Q_{ij}}{\partial r_k}, \ i, j, k = 1, 2, 3, \ f_B(\mathbf{Q}) := \frac{A}{2} \mathrm{tr} \mathbf{Q}^2 - \frac{B}{3} \mathrm{tr} \mathbf{Q}^3 + \frac{C}{4} (\mathrm{tr} \mathbf{Q}^2)^2 - f_{B,0}. \tag{3}$$

More precisely, the working domain is a cuboid $V = [-\lambda, \lambda]^2 \times [-\lambda h, \lambda h]$ where $\lambda$ is edge-length of the 2D square cross-section and $h$ is a measure of the height ($h > 0$); $L > 0$ is a material-dependent elastic constant, $A = \alpha(T - T^*)$ is the rescaled temperature, with $\alpha > 0$ and $T^*$ is a characteristic liquid crystal temperature; $B, C > 0$ are material-dependent bulk constants. The minimizers of $f_B$ depend on $A$, and determine the NLC phase for spatially homogeneous samples. When $A > \frac{B^2}{24C}$, the minimizer of $f_B$ is the isotropic state, and for $A < 0$, the minimizers of $f_B$ constitute a continuum of uniaxial $\mathbf{Q}$-tensors defined by

$$\mathcal{N} = \left\{ \mathbf{Q} = s_+ \left( \mathbf{n} \otimes \mathbf{n} - \frac{\mathbf{I}}{3} \right) \right\},$$

where

$$s_+ = \frac{B + \sqrt{B^2 - 24AC}}{4C},$$

and $\mathbf{n}$ is an arbitrary unit vector field that models the uniaxial director.

By rescaling the system according to $(\bar{x}, \bar{y}, \bar{z}) = (\frac{x}{\lambda}, \frac{y}{\lambda}, \frac{z}{\lambda})$, $\bar{\lambda}^2 = \frac{2C\lambda^2}{L}$ and dropping the bars in subsequent discussions (so that all results are in terms of dimensionless variables), the non-dimensionalized LdG free energy is given by,

$$E[\mathbf{Q}] := \int_V \left[ \frac{1}{2} |\nabla \mathbf{Q}|^2 + \lambda^2 \left( \frac{A}{4C} \mathrm{tr} \mathbf{Q}^2 - \frac{B}{6C} \mathrm{tr} \mathbf{Q}^3 + \frac{1}{8} \mathrm{tr} \mathbf{Q}^2)^2 - \frac{f_{B,0}}{2C} \right) \right] \mathrm{d}A. \tag{4}$$

The normalized domain is $V = \Omega \times [-h, h]$, $\Omega = [-1, 1]^2$ is the two-dimensional cross-section of the cuboid, and $\lambda^2$ describes the cross-sectional size. In what follows, we take fixed values of the parameters $B = 0.64 \times 10^4 \mathrm{Nm}^{-2}$, $C = 0.35 \times 10^4 \mathrm{Nm}^{-2}$, and $L = 4 \times 10^{-11} \mathrm{N}$, which roughly correspond to the commonly used NLC material, MBBA [28, 29]. We focus on a special temperature $A = -B^2/3C$, which is a representative low temperature, to largely facilitate comparison with 2D results in [11, 17]. Then $f_{B,0} = \frac{A}{3} s_+^2 - \frac{2B}{27} s_+^3 + \frac{C}{9} s_+^4$ with $s_+ = B/C$ [29], is added to ensure a non-negative energy density.

Of prime importance are nematic defects which have distinct optical signatures under a polarizing microscope [1] and can be used to label families of LdG critical points. Motivated by the results in [14], we use an innovative measure to identify defects. At the special temperature $A = -B^2/3C$, we have a branch of LdG critical points, $\mathbf{Q}_c$, with $q_4 = q_5 = 0$ and constant $q_3 = -\frac{B}{6C}$, i.e.

$$\mathbf{Q}_c = q(x, y, z) \left( \mathbf{n}_1 \otimes \mathbf{n}_1 - \mathbf{n}_2 \otimes \mathbf{n}_2 \right) - \frac{B}{6C} \left( 2\mathbf{z} \otimes \mathbf{z} - \mathbf{n}_1 \otimes \mathbf{n}_1 - \mathbf{n}_2 \otimes \mathbf{n}_2 \right), \qquad (5)$$

where $\mathbf{n}_1(x, y, z)$ is a 2D nematic director in the square plane, and $\mathbf{z}$ is the unit-vector in the $z$-direction [12]. These critical points only have 2 degrees of freedom, $q$ and a degree of freedom associated with $\mathbf{n}_1$, such that $\mathbf{n}_1$ and $\mathbf{n}_2$ are orthogonal 2D unit vectors. For such critical points, the defect set is identified with the nodal set of $q$ i.e. a set of no order in the cross-sectional planes of the cuboid. Whilst solving for all five degrees of freedom, we numerically recover a class of critical points with only two degrees of freedom as above, and the $z$-dependence of $q$ and $\mathbf{n}_1$ generates the novel $z$-variant 3D LdG critical points. Hence, for LdG critical points with only two degrees of freedom as above, we use $\lambda_3 - B/6C$ ($\lambda_3$ is the maximum eigenvalue of $\mathbf{Q}$) to visualize the location of defects [17, 19, 21]. We use the colorbar, $\lambda_3 - B/6C$, in Sections 4.1-4.5.

For critical points with out-of-plane directors that exploit the full five degrees of freedom, defects can be tracked by the isosurface of biaxiality parameter $\beta^2 = 1 - 6\mathrm{tr}(\mathbf{Q}^3)^2/(\mathrm{tr}(\mathbf{Q}^2))^3$, $0 \leqslant \beta \leqslant 1$. We have $\beta^2 = 0$ if and only if $\mathbf{Q}$ is uniaxial or isotropic [30], and hence, we use the biaxiality parameter, $\beta^2$ to track defects in Sec. 4.6, which focuses on escaped critical points.

With regards to boundary conditions, we use tangent Dirichlet boundary conditions on the lateral surfaces and Neumann boundary conditions on the top and bottom surfaces of the cuboid. The tangent Dirichlet conditions require the leading nematic director (with the largest positive eigenvalue) to be tangent to the edges of the 2D cross-section, $\Omega$ of the 3D cuboid. This creates a natural mismatch at the four vertices of $\Omega$. Following the linear interpolation approach in [14, 21, 31], we define the Dirichlet condition, $\mathbf{Q} = \mathbf{Q}_{bc}$ on the lateral surfaces, $x = \pm 1$ and $y = \pm 1$, in terms of a function
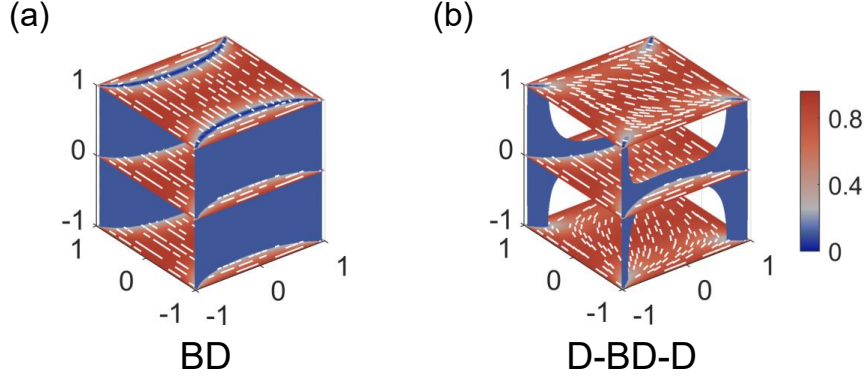
**Figure 1.** The plot of (a) $z$-invariant boundary distortion (BD) state and (b) $z$-variant D-BD-D state [24]. The name of D-BD-D indicates that it displays D (Diagonal), BD (Boundary Distortion), and D profiles on the top, middle, and bottom slices, respectively. The color bar and the white lines label the scalar order parameter and the director. The blue regions ($\lambda_3 - B/6C < 0.1$) represent the NLC defects and we omit it in some following figures for better visualization.

with a shape parameter,

$$
\begin{cases}
\mathbf{Q}_{bc}(x = \pm 1, y, z) = \frac{s_+}{3} \begin{pmatrix} -T_\epsilon(y) & 0 & 0 \\ 0 & 2T_\epsilon(y) & 0 \\ 0 & 0 & -T_\epsilon(y) \end{pmatrix}, \\[20pt]
\mathbf{Q}_{bc}(x, y = \pm 1, z) = \frac{s_+}{3} \begin{pmatrix} 2T_\epsilon(x) & 0 & 0 \\ 0 & -T_\epsilon(x) & 0 \\ 0 & 0 & -T_\epsilon(x) \end{pmatrix},
\end{cases} \tag{6}
$$

where

$$
T_\epsilon(t) = \begin{cases} (1+t)/\epsilon, & -1 \leqslant t \leqslant -1 + \epsilon, \\ 1, & |t| \leqslant 1 - \epsilon, \\ (1-t)/\epsilon, & 1 - \epsilon \leqslant t \leqslant 1. \end{cases} \tag{7}
$$

We take a sufficiently small $0 < \epsilon \ll 1$, and the qualitative solution profiles are not changed by the choice of the interpolation. The Neumann boundary conditions

$$
\frac{\partial \mathbf{Q}}{\partial n} = 0, \ z = \{-h, h\}, \ (x, y) \in \Omega, \tag{8}
$$

where $n$ is the normal vector, allow for $z$-invariant states i.e. NLC states which are invariant across the height of the cuboid (see Fig. 1(a)).

The critical points of the LdG free energy in (4) are classical solutions of the corresponding Euler-Lagrange equations:

$$
\Delta \mathbf{Q} = \lambda^2 \left( \frac{A}{2C} \mathbf{Q} - \frac{B}{2C} \left( \mathbf{Q}^2 - \frac{tr(\mathbf{Q})^2}{3} \mathbf{I} \right) + \frac{1}{2} tr(\mathbf{Q})^2 \mathbf{Q} \right), \tag{9}
$$

with the imposed boundary conditions on the lateral surfaces (6), and natural boundary conditions in (8). The energy minimizers model the physically observable states, and there are a plethora of non energy-minimizing solutions of (9). In what follows, we study the relationships between the non energy-minimizing and energy-minimizing solutions of (9), and how the solution connectivity can be used to construct 3D NLC configurations on a cuboid. The cuboid is a generic and physically relevant example and our methods can be generalized to arbitrary 3D geometries.

## 3. Numerical method

In this section, we describe the numerical methods used to compute the critical points of the LdG free energy in (4), with special attention to the non energy-minimizing critical points which are typically hard to find. The critical points, $\mathbf{Q}$, are solutions of the Euler-Lagrange equations (9), which are a system of five nonlinear partial differential equations, for the five components of the $\mathbf{Q}$-tensor in (1) and we solve for all 5 degrees of freedom, $q_1, \ldots, q_5$.

A critical point of the LdG free energy, $\hat{\mathbf{Q}}$ is stable if the Hessian of the associated LdG free energy, $\nabla^2 E(\hat{\mathbf{Q}})$, has only positive eigenvalues, and unstable if it has a negative eigenvalue. We study unstable saddle points of the LdG free energy, that are unstable in specific eigendirections. More precisely, for a non-degenerate index-$k$ (Morse index) saddle point $\hat{\mathbf{Q}}$, the Hessian $\nabla^2 E(\hat{\mathbf{Q}})$ has exactly $k$ negative eigenvalues: $\lambda_1 \leqslant \cdots \leqslant \lambda_k$, corresponding to $k$ unit eigenvectors $\hat{\mathbf{v}}_1, \cdots, \hat{\mathbf{v}}_k$ subject to $\langle \hat{\mathbf{v}}_i, \hat{\mathbf{v}}_j \rangle = \delta_{ij}$, $1 \leqslant i, j \leqslant k$. A stable critical point $\hat{\mathbf{Q}}$ is an index-0 critical point, i.e., the smallest eigenvalue of $\nabla^2 E(\hat{\mathbf{Q}})$ is positive. While a stable state can be relatively easily found by gradient descent method using a proper initial guess, finding a transition state (an index-1 saddle point) or high-index saddle points is much more difficult. There are numerical methods for the computation of transition pathways mediated by index-1 saddle points, e.g. string methods [32, 33], but they largely depend on a proper initial guess. However, initial guesses for saddle points are not easy to find since we typically do not have a priori knowledge of saddle points on the energy landscape. In what follows, we review the method of saddle dynamics and propose a hybrid numerical scheme to circumvent numerical stiffness and convergence issues.

### 3.1. Saddle dynamics

The saddle dynamics (SD) method [34, 35, 36] has been successfully used to efficiently compute the LdG critical points on 2D domain [19, 21, 37]. We review the SD method in the following. The SD for an index-$k$ saddle point $\mathbf{Q}$ (denoted by $k$-SD) is defined to

be,

$$
\begin{cases}
\dot{\mathbf{Q}} = -(\mathbf{I} - 2\sum_{i=1}^{k}\mathbf{v}_i\mathbf{v}_i^\top)\nabla E(\mathbf{Q}), \\[2ex]
\dot{\mathbf{v}}_i = -(\mathbf{I} - \mathbf{v}_i\mathbf{v}_i^\top - \sum_{i=1}^{i-1}2\mathbf{v}_j\mathbf{v}_j^\top)\nabla^2 E(\mathbf{Q})\mathbf{v}_i, \ i = 1, 2, \cdots, k,
\end{cases}
\tag{10}
$$

where $\mathbf{I}$ is the identity operator. To avoid evaluating the Hessian of $E(\mathbf{Q})$, we use the dimer

$$
h(\mathbf{Q}, \mathbf{v}_i) = \frac{\nabla E(\mathbf{Q} + l\mathbf{v}_i) - \nabla E(\mathbf{Q} - l\mathbf{v}_i)}{2l}
\tag{11}
$$

as an approximation of $\nabla^2 E(\mathbf{Q})\mathbf{v}_i$, with a small dimer length $2l$. By setting the $k$-dimensional subspace $\mathcal{V} = \mathrm{span}\{\hat{\mathbf{v}}_1, \cdots, \hat{\mathbf{v}}_k\}$, $\hat{\mathbf{Q}}$ is a local maximum on $\hat{\mathbf{Q}} + \mathcal{V}$ and a local minimum on $\hat{\mathbf{Q}} + \mathcal{V}^\perp$, where $\mathcal{V}^\perp$ is the orthogonal complement of $\mathcal{V}$. The dynamics for $\mathbf{Q}$ in (10) can be written as

$$
\begin{aligned}
\dot{\mathbf{Q}} &= \left(\mathbf{I} - \sum_{i=1}^{k}\mathbf{v}_i\mathbf{v}_i^\top\right)(-\nabla E(\mathbf{Q})) + \left(\sum_{i=1}^{k}\mathbf{v}_i\mathbf{v}_i^\top\right)\nabla E(\mathbf{Q}) \\
&= (\mathbf{I} - \mathcal{P}_\mathcal{V})(-\nabla E(\mathbf{Q})) + \mathcal{P}_\mathcal{V}(\nabla E(\mathbf{Q})),
\end{aligned}
\tag{12}
$$

where $\mathcal{P}_\mathcal{V}\nabla E(\mathbf{Q}) = \left(\sum_{i=1}^{k}\mathbf{v}_i\mathbf{v}_i^\top\right)\nabla E(\mathbf{Q})$ is the orthogonal projection of $\nabla E(\mathbf{Q})$ on $\mathcal{V}$. Thus, $(\mathbf{I} - \mathcal{P}_\mathcal{V})(-\nabla E(\mathbf{Q}))$ is a descent direction on $\mathcal{V}^\perp$, and $\mathcal{P}_\mathcal{V}(\nabla E(\mathbf{Q}))$ is an ascent direction on $\mathcal{V}$.

The dynamics for $\mathbf{v}_i, i = 1, 2, \cdots, k$ in (10) can be obtained by minimizing the $k$ Rayleigh quotients simultaneously with the gradient type dynamics,

$$
\min_{\mathbf{v}_i} \ \langle \mathbf{v}_i, \nabla^2 E(\mathbf{Q})\mathbf{v}_i \rangle, \ \text{s.t.} \ \langle \mathbf{v}_i, \mathbf{v}_j \rangle = \delta_{ij}, \ j = 1, 2, \cdots, i,
\tag{13}
$$

which generates the subspace $\mathcal{V}$ by computing the eigenvectors corresponding to the smallest $k$ eigenvalues of $\nabla^2 E(\mathbf{Q})$.

### 3.2. Hybrid numerical scheme

We label hierarchies of LdG saddle points in a 3D cuboid by A-B-C, where A, B and C are the 2D profiles on $z = h$, $z = 0$ and $z = -h$. We conjecture that when $h$ is large enough, we can move the middle state, generically denoted by $B$, up and down, without a significant energetic cost. If one eigenvalue, $\lambda_{\min}$ is close to zero (Fig. 2), then this will cause numerical issues including the stiffness and slow convergence of the saddle dynamics.

We elaborate on the numerical issues further by using $k$-saddle dynamics to find a target saddle point $\mathbf{Q}^*$, for which the smallest absolute eigenvalue, $\lambda_1$ is such that $|\lambda_1| < \epsilon$ and we consider the Jacobian operator of $k$-saddle dynamics,
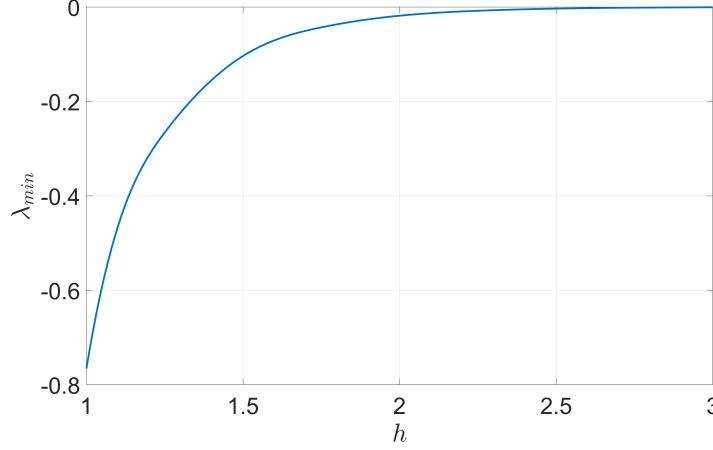
**Figure 2.** The smallest eigenvalue of D-BD-D versus $h$ at $\lambda^2 = 30$.

$$\mathbf{J}(\mathbf{Q}, \mathbf{v}_1, \cdots, \mathbf{v}_k) = \frac{\partial(\dot{\mathbf{Q}}, \dot{\mathbf{v}}_1, \cdots, \dot{\mathbf{v}}_k)}{\partial(\mathbf{Q}, \mathbf{v}_1, \cdots, \mathbf{v}_k)} = \begin{pmatrix} \mathbf{J_Q} & \mathbf{J_{Q1}} & \mathbf{J_{Q2}} & \cdots & \mathbf{J_{Q}}_k \\ \mathbf{J_{1Q}} & * & \mathbf{0} & \cdots & \mathbf{0} \\ \mathbf{J_{2Q}} & * & * & \cdots & \mathbf{0} \\ \vdots & \vdots & \vdots & & \vdots \\ \mathbf{J_{kQ}} & * & * & \cdots & * \end{pmatrix} \tag{14}$$

where

$$\mathbf{J_Q} = \frac{\partial \dot{\mathbf{Q}}}{\partial \mathbf{Q}} = - \left( \mathbf{I} - \sum_{i=1}^{i=k} 2\mathbf{v}_i \mathbf{v}_i^\top \right) \nabla^2 E(\mathbf{Q}), \tag{15}$$

$$\mathbf{J_{Q}}_i = \frac{\partial \dot{\mathbf{Q}}}{\partial \mathbf{v}_i} = -2 \left( \mathbf{v}_i^\top \nabla E(\mathbf{Q}) \mathbf{I} + \mathbf{v}_i \nabla E(\mathbf{Q})^\top \right). \tag{16}$$

Now, we consider the spectral decomposition of $\nabla^2 E(\mathbf{Q}^*)$,

$$\nabla^2 E(\mathbf{Q}^*) = \sum_{i=1}^{i=m} \lambda_i \mathbf{v}_i^* \mathbf{v}_i^{*\top}, |\lambda_1| \leqslant |\lambda_2| \leqslant \cdots \leqslant |\lambda_m|. \tag{17}$$

Note that $\nabla E(\mathbf{Q}^*) = 0$, consequently,

$$\mathbf{J}(\mathbf{Q}^*, \mathbf{v}_{j_1}^*, \cdots, \mathbf{v}_{j_k}^*) = \frac{\partial(\dot{\mathbf{Q}}^*, \dot{\mathbf{v}}_{j_1}^*, \cdots, \dot{\mathbf{v}}_{j_k}^*)}{\partial(\mathbf{Q}^*, \mathbf{v}_{j_1}^*, \cdots, \mathbf{v}_{j_k}^*)} = \begin{pmatrix} \mathbf{J_{Q^*}} & \mathbf{0} & \mathbf{0} & \cdots & \mathbf{0} \\ \mathbf{J_{1Q^*}} & * & \mathbf{0} & \cdots & \mathbf{0} \\ \mathbf{J_{2Q^*}} & * & * & \cdots & \mathbf{0} \\ \vdots & \vdots & \vdots & & \vdots \\ \mathbf{J_{kQ^*}} & * & * & \cdots & * \end{pmatrix} \tag{18}$$

$$\mathbf{J_{Q^*}} = - \left( \mathbf{I} - \sum_{i=j_1}^{i=j_k} 2\mathbf{v}_i^* \mathbf{v}_i^{*\top} \right) \sum_{i=1}^{i=m} \lambda_i \mathbf{v}_i^* \mathbf{v}_i^{*\top} = \sum_{i=1}^{i=m} (-1)^{\alpha(i)} \lambda_i \mathbf{v}_i^* \mathbf{v}_i^{*\top}, \tag{19}$$

where $j_i, i = 1, \cdots, k$ are the subscripts corresponding to negative eigenvalues and $\alpha$ is the indicator function of the set $\{j_i, i = 1, \cdots, k\}$. Thus, $\text{Cond}_2(\mathbf{J}(\mathbf{Q}^*)) \geqslant$

$\text{Cond}_2(\mathbf{J}_{\mathbf{Q}^*}) = |\lambda_m|/|\lambda_1|$, which is relatively large due to the smallness of $\lambda_1$, i.e., the $k$-saddle dynamics is stiff when the iteration point is close to $\mathbf{Q}^*$. Consequently, the saddle dynamics offers high impedance to $\mathbf{v}_1^*$. In fact, the saddle dynamics (10) is a special gradient method and it exhibits the "jagged phenomenon", i.e., the iteration point will slowly move along eigenvector corresponding to the smallest absolute eigenvalue. The convergence rate is largely dependent on the degree of separation between $|\lambda_1|$ and $|\lambda_m|$. These numerical difficulties motivate us to develop a suitable numerical method to accelerate (10).

The large stiffness of (10) necessitates an absolutely stable (A-stable) scheme. The linear term in (10) is implicit for numerical stability. The nonlinear term, $|\mathbf{Q}|^2\mathbf{Q}$, is also semi-implicitly discretized in time direction as $|\mathbf{Q}^n|^2\mathbf{Q}^{n+1}$ for better numerical stability. The term $|\mathbf{Q}^n|^2\mathbf{Q}^{n+1}$ is very beneficial for solving linear equations in the semi-implicit scheme, because it is a positive definite term of the diagonal elements. Instead of re-generating unstable eigendirections with the gradient type dynamics in (10), we apply a single-step Locally Optimal Block Preconditioned Conjugate Gradient (LOBPCG) method [38] to calculate the unstable eigendirections, and the Hessians are also approximated by dimers [34]. The semi-implicit scheme is given by,

$$
\begin{cases}
\dfrac{\mathbf{Q}_{n+1} - \mathbf{Q}_n}{\Delta t_n} = \Delta_{\delta x}\mathbf{Q}_{n+1} - \lambda^2\left(\dfrac{A}{2C}\mathbf{Q}_{n+1} + \dfrac{1}{2}|\mathbf{Q}_n|^2\mathbf{Q}_{n+1} - \dfrac{B}{2C}\left({\mathbf{Q}_n}^2 - \dfrac{|\mathbf{Q}_n|^2}{3}\mathbf{I}\right)\right) \\
\qquad\qquad + (2\displaystyle\sum_{i=1}^{k}\mathbf{v}_{n,i}\mathbf{v}_{n,i}^\top)\nabla_{\delta x}E(\mathbf{Q}_n), \\
\text{Renew } \mathbf{v}_{n,i} \text{ as } \mathbf{v}_{n+1,i} \text{ with single-step LOBPCG, } i = 1, 2, \cdots, k.
\end{cases}
$$
$$(20)$$

This semi-implicit scheme is A-stable and it allows us to choose a large step size, which suffices for our purpose. We use finite difference methods to estimate the spatial derivatives in (20) with mesh size $\delta x = 1/32$. We have tested that the solutions are not sensitive to smaller choices of $\delta x$ by refining the mesh size.

The convergence rate is still slow due to the small eigenvalue, even with a large time step. We use Newton's method to accelerate the tail convergence, i.e., when the gradient is large, the saddle dynamics is used to ensure that $\mathbf{Q}_n$ falls into the basin of attraction of $\mathbf{Q}^*$, and then Newton's method pushes $\mathbf{Q}_n$ to $\mathbf{Q}^*$, with a higher convergence rate. However, Newton's method requires solving a large sparse ill-conditioned linear system, $R_n = \nabla^2 E(\mathbf{Q}_n)\delta\mathbf{Q} + \nabla E(\mathbf{Q}_n) = 0$, at each step, and we hence, choose the Inexact-Newton method, i.e., give $R_n$ a tolerance $\|R_n\| \leqslant \eta_n\|\nabla E(\mathbf{Q}_n)\|$ with $\eta_n < 1$. When the linear system is not very ill-conditioned ($\text{Cond}_2(\nabla^2 E(\mathbf{Q}_n) \leqslant 10^8$), it can be solved within this tolerance by iteration methods, e.g., the generalized minimal residual method (GMRES) and symmetric successive over-relaxation method (SSOR). A small $\eta_n$ achieves faster convergence but leads to more expensive computational costs to solve the linear system. When $\mathbf{Q}_n$ is not too close to $\mathbf{Q}^*$, the matrix is not heavily ill-conditioned and we can solve the linear system more exactly to accelerate

the convergence and keep $\mathbf{Q}_n$ in the basin of attraction of $\mathbf{Q}^*$; when $\mathbf{Q}_n$ is close to $\mathbf{Q}^*$, we choose a larger $\eta_n$ to save computational cost. Combining these considerations, we choose $\eta_n = \min(C, \bar{\eta}_n), \bar{\eta}_n = \frac{1}{1+100\|\nabla E(\mathbf{Q}_n)\|}$ , and $0 < C < 1$ is a constant to guarantee at least linear convergence rate. In our numerical calculations, the calculation speed is more sensitive to the choice of $C$, a small $C$ is more efficient when $h$ is relatively small.

We solve five large sparse linear systems (five degrees of freedom) in (20) at every time step, and the single-step LOBPCG needs another $4k$ derivative evaluations, which is computationally expensive, particularly for finding higher-index saddle points. Fortunately, we can use the explicit scheme combined with the Barzilai-Borwein step size [39] to save the computational cost at the beginning of the iteration. Thus, we use the explicit system, combined with the semi-implicit scheme and the Inexact-Newton method to propose the final hybrid numerical scheme:

$$\begin{cases} \text{The explicit scheme of (10), } \|\nabla E(\mathbf{Q}_n)\| \geqslant \mu \text{ and } n \leqslant N, \\ \text{The semi-implicit scheme (20), } \|\nabla E(\mathbf{Q}_n)\| \geqslant \mu \text{ and } n > N, \\ \mathbf{Q}_{n+1} = \mathbf{Q}_n + \delta\mathbf{Q}, \|\nabla^2 E(\mathbf{Q}_n)\delta\mathbf{Q} + \nabla E(\mathbf{Q}_n)\| \leqslant \eta_n\|\nabla E(\mathbf{Q}_n)\| \text{ ,Oherwise,} \end{cases} \tag{21}$$

where $N$ is a step parameter to automatically identify the stiffness of (10). For the well-conditioned case (Fig. 3(a)), the iteration point can reach $\|\nabla E(\mathbf{Q}_n)\| < \mu$ within the step parameter, by means of the explicit scheme alone, and then Inexact-Newton method pushes convergence to the saddle point. For ill-conditioned cases (Fig. 3(b)), the explicit scheme cannot achieve $\|\nabla E(\mathbf{Q}_n)\| < \mu$ within the step parameter, and the semi-implicit scheme is used to achieve $\|\nabla E(\mathbf{Q}_n)\| < \mu$ followed by the Inexact-Newton method to complete tail convergence.
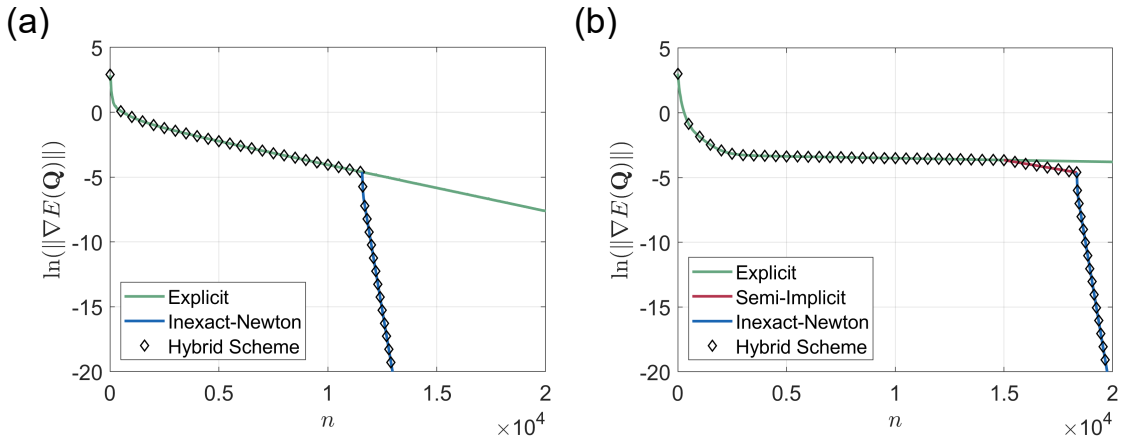


**Figure 3.** The upward search for finding the index-1 D-BD-D from the stable D state by following the 1-SD (the initial condition is D+0.5*$(\mathbf{v}_1 + \mathbf{v}_2)$) with (a) $h = 1$ and (b) $h = 2$. The parameters in (21) are $\mu = 10^{-2}, N = 15000, C = 0.99$.

*Hierarchies of Critical Points of a Landau-de Gennes Free Energy*      13

### 3.3. Construction of the solution landscape

The solution landscape is an umbrella term used to describe the collection of unstable saddle points and stable critical points of the LdG free energy. Crucially, the solution landscape contains penetrating information about the pathways between critical points: how high-index saddle points are connected to low-index saddle points, and eventually to index-0 stable critical points. Solution landscapes contain crucial information about the connectivity of a system, and can track how the unstable and stable eigendirections evolve as we connect the different critical points, noting that not all critical points can be connected.

Following the discrete SD dynamics (21), we can construct the solution landscape without tuning initial guesses, by two algorithms: the downward search that enables us to search for connected index-$s$ saddle points from known index-$s$ $(k > s)$ saddles $(\mathbf{Q}, \mathbf{v}_1, \mathbf{v}_2, \cdots, \mathbf{v}_k)$, two typical choices for the initial guess of $s$-SD are $(\mathbf{Q} \pm \epsilon \mathbf{v}_{s+1}, \mathbf{v}_1, \mathbf{v}_2, \cdots, \mathbf{v}_s)$; the upward search to find connected index-k saddle points from known index-$s$ $(k > s)$ saddles $(\mathbf{Q}, \mathbf{v}_1, \mathbf{v}_2, \cdots, \mathbf{v}_s, \bar{\mathbf{v}}_{s+1}, \cdots, \bar{\mathbf{v}}_k)$, where $\bar{\mathbf{v}}_i, i = s+1, \cdots, k$ are stable eigenvectors of $\mathbf{Q}$, two typical choices for the initial guess of the $k$-SD are $(\mathbf{Q} \pm \epsilon \bar{\mathbf{v}}_{s+1}, \mathbf{v}_1, \mathbf{v}_2, \cdots, \mathbf{v}_s, \bar{\mathbf{v}}_{s+1}, \cdots, \bar{\mathbf{v}}_k)$ [17, 40]. In the next section, we present our numerical results, based on this hybrid numerical scheme for solution landscapes.

## 4. Results

### 4.1. z-invariant LdG critical point (A-A-A)

In [16], the authors study LdG critical points on a square domain, with edge length $\lambda$ and tangent boundary conditions, and study how the critical points depend on $\lambda$. For $\lambda$ small enough, there is a unique critical point, coined as the Well Order Reconstruction Solution (WORS), which is also the unique energy minimizer. The $\mathbf{Q}$-tensor of WORS has a constant set of eigenvectors, and is distinguished by a uniaxial cross with negative scalar order parameter, along the diagonals i.e. the corresponding $\mathbf{Q}$ is of the form $\mathbf{Q}_u = s \left( \mathbf{n} \otimes \mathbf{n} - \frac{\mathbf{I}}{3} \right)$ with $s < 0$, on the square diagonals. Physically, this means that there is a planar defect cross along the square diagonals such that the NLC molecules are disordered in the square plane, on the diagonals. In [10], the authors analyze the WORS at the special temperature $A = -B^2/3C$ and show that the WORS critical point is defined by

$$\mathbf{Q}_{WORS} = q(\hat{\mathbf{x}} \otimes \hat{\mathbf{x}} - \hat{\mathbf{y}} \otimes \hat{\mathbf{y}}) - \frac{B}{6C}(2\hat{\mathbf{z}} \otimes \hat{\mathbf{z}} - \hat{\mathbf{x}} \otimes \hat{\mathbf{x}} - \hat{\mathbf{y}} \otimes \hat{\mathbf{y}})$$

where $\hat{\mathbf{x}}$, $\hat{\mathbf{y}}$, $\hat{\mathbf{z}}$ are the unit-vectors in the coordinate directions, and $q$ is a solution of the Allen-Cahn equation with prescribed boundary conditions.

The WORS exists as a 2D LdG critical point on all square domains, for all $\lambda$. One can numerically show the smallest eigenvalue of the Hessian of the LdG energy, at the WORS critical point, on $\Omega$, is strictly decreasing with increasing $\lambda$. At the first bifurcation point, $\lambda = \lambda^*$, the 2D WORS becomes an index-1 saddle point and bifurcates

into two stable D solutions. The D solutions are approximately uniaxial with the uniaxial director along one of the square diagonals. There are two rotationally equivalent D solutions. At the second bifurcation point $\lambda = \lambda^{**}$, the index-1 WORS bifurcates into an index-2 WORS with two unstable eigenvectors, $\mathbf{v}_1$ and $\mathbf{v}_2$, and two boundary distortion (BD) solutions appear at approximately $\lambda^2 = 15$. With the disturbance along $\mathbf{v}_1$ on WORS, the leading eigenvector aligns along a square diagonal and the WORS relaxes ("relax" refers to following either gradient flow or saddle dynamics) to a D state. With the disturbance along $\mathbf{v_2}$, the diagonal cross for the WORS is pulled apart, leading to two planar line defects near a pair of opposite square edges, relaxing into a BD state. A defect line is interpreted to be a line with no planar nematic order in the square plane, i.e., isotropic lines in the square plane but note that $\mathbf{Q} \neq \mathbf{0}$ along the defect lines, since there is negative uniaxial ordering along $\mathbf{z}$-the normal to the square domain. Each unstable BD further bifurcates into two unstable R solutions, where each R solution is approximately uniaxial such that the uniaxial director rotates by $\pi$-radians between a pair of opposite square edge. As $\lambda$ further increases, the unstable R solutions gain stability, and we have 4 rotationally equivalent R solutions related to each other by $\pi/2$-rotations.

In what follows, we use this catalogue of 2D LdG critical points - WORS, BD, D and R, to construct 3D critical points on the 3D cuboid. These 2D LdG critical points exist as $z$-invariant 3D critical points i.e. critical points of the form

$$\mathbf{Q}_{3D}(x,y,z) = \mathbf{Q}_{2D}\left(x,y,-h\right) \quad \forall x,y \in \Omega, \ z \in [-h,h],$$

and in this section, we study the $z$-invariant 3D WORS critical point on a 3D cuboid with cross-sectional edge length, $\lambda$, and height $h$. We show that there are differences between the 2D and 3D cases, even when restricted to $z$-invariant LdG critical points.



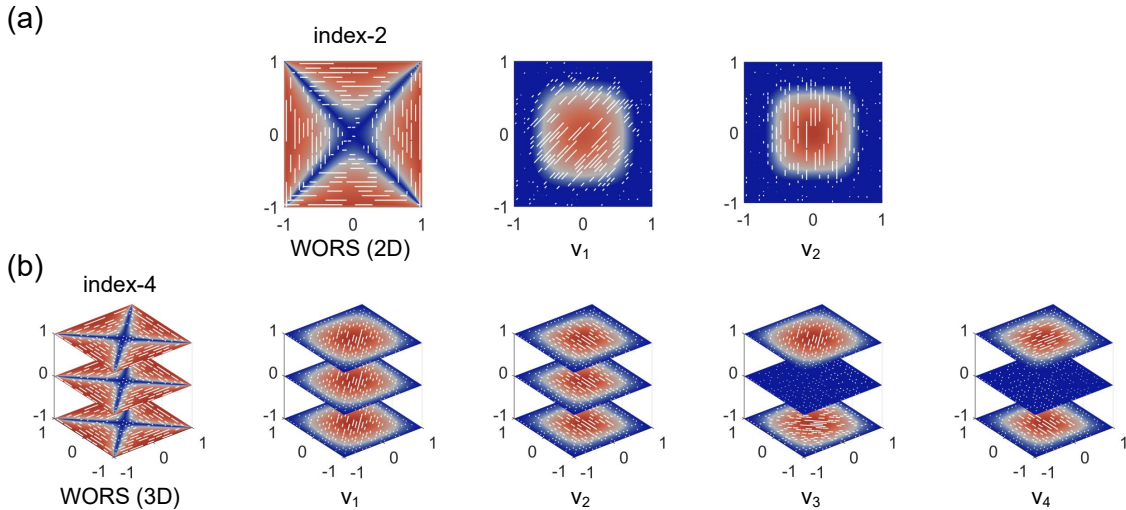**Figure 4.** (a) The 2D WORS computed on $\Omega$, and its unstable eigenvectors at $\lambda^2 = 15$. (b) The 3D WORS with its unstable eigenvectors $v_1, \cdots, v_4$ with $\lambda^2 = 15, h = 1$.

**Table 1.** The index of 2D and 3D ($h = 1$) WORS versus $\lambda^2$. $N_{z-variant}$ is the number of unstable $z$-variant eigenvector of WORS, i.e., the index of 3D WORS minus the index of 2D WORS.

| $\lambda^2$ | 2 | 7 | 10 | 12 | 15 | 19 | 22 | 30 |
|---|---|---|---|---|---|---|---|---|
| index of 2D WORS | 0 | 1 | 2 | 2 | 2 | 4 | 4 | 4 |
| index of 3D WORS | 0 | 1 | 2 | 3 | 4 | 6 | 7 | 10 |
| $N_{z-variant}$ | 0 | 0 | 0 | 1 | 2 | 2 | 3 | 6 |

The 3D WORS is a $z$-invariant 3D LdG critical point (see Fig. 4(b)) for all $\lambda$ and $h$, with the boundary conditions specified in (6). The 3D WORS is the global energy minimizer for sufficiently small $\lambda$ [24]. In other words, WORS-type solutions are not a 2D-artefact. By analogy with the 2D case, the 3D WORS loses stability as $\lambda$ increases, for a fixed $h$. In fact, for a fixed $\lambda$ and $h = 1$, we numerically observe that the index of the 3D $z$-invariant WORS is always greater than or equal to the index of the 2D WORS. For example, the 3D WORS is an index-4 saddle point at $\lambda^2 = 15, h = 1$ with two $z$-invariant unstable eigenvectors as in the 2D case. One can verify that the eigenvectors of a 2D LdG critical point are also the eigenvectors of the corresponding $z$-invariant 3D LdG critical point. However, the 3D WORS can also accommodate unstable $z$-variant eigenvectors like $\mathbf{v}_3$ and $\mathbf{v}_4$ as shown in Fig. 4(b). With the disturbance along $\mathbf{v}_3$ ($\mathbf{v}_4$) on WORS, the top surface ($z = h$) relaxes to a D (BD) state and the bottom surface ($z = -h$) relaxes to another D (BD) state, while the middle slice retains the WORS profile. As $\lambda$ increases, the 3D $z$-invariant WORS critical point has an increasing number of $z$-variant eigenvectors (which cannot be accommodated in the 2D case) and hence, this intuitively explains why the 3D $z$-invariant WORS has a higher Morse index than its 2D counterpart, for $\lambda$ is large enough, some of which is tabulated in Table 1.

*4.2. 3D LdG critical points constructed by 2D pathways (A1-B-A2)*

This subsection is devoted to numerical examples that illustrate the relationships between solution landscapes on a 2D square and a 3D cuboid, i.e. examples that exemplify the effect of the third dimension. In Fig. 5, we construct the solution landscape on a 2D square and a 3D cuboid at $\lambda^2 = 19$. Here, the 2D WORS is an index-4 saddle point. Following the 3-SD along $\mathbf{v}_4$, a T state (there are four T states if symmetry is taken into account) is numerically computed, and an index-2 H state can be obtained from the T state following 2-SD dynamics. Further, the H state relaxes to the index-1 BD state, and the BD state relaxes to the stable D state, which is the global energy minimum.

Next, we consider the solution landscape on a cuboid or a 3D well with $\lambda^2 = 19$ and $h = 1$. The 3D WORS is an index-6 saddle point, with two unstable $z$-variant eigenvectors. We can naturally observe the connectivity between the 2D saddle points as 3D $z$-invariant saddle points on a cuboid. For example, the 3D $z$-invariant WORS
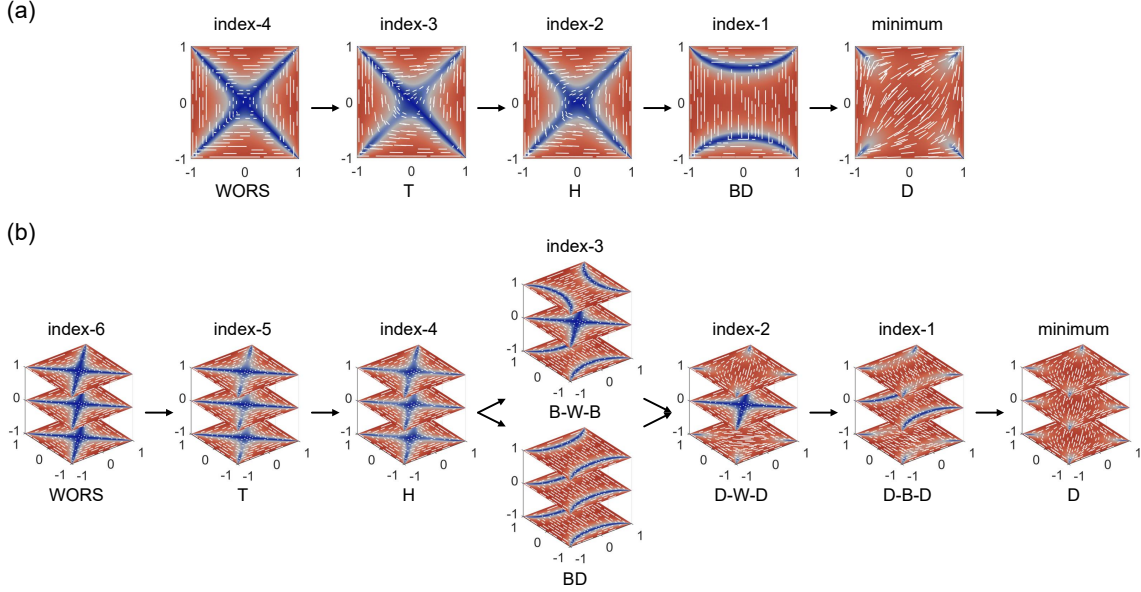
**Figure 5.** The solution landscape on (a) 2D square and (b) 3D cube at $\lambda^2 = 19$. The arrow from the higher-index saddle to the lower-index saddle represents a downward search, that is, the solution (in the arrow's tail) with a small perturbation is able to converge to the solution in the arrow's head by following the SD in (10). In terms of nomenclature, B and W are the shorthand of BD and WORS, respectively.

relaxes to the 3D $z$-invariant T state and then the $z$-invariant 3D H state, and further the $z$-invariant 3D BD state by following the unstable eigenvectors. However, we also observe $z$-variant 3D LdG critical points which cannot be observed in the 2D scenario. The $z$-invariant 3D saddle points are connected to $z$-variant 3D LdG critical points, so that 3D solution landscapes offer multiple routes for tuning system properties. For example, we observe that the $z$-invariant 3D H state relaxes to the $z$-variant B-W-B saddle point, for which the top surface exhibits the BD profile, the middle slice supports the WORS profile and the bottom surface is the other BD profile (related by $\pi/2$ coordinate rotation). We can use the 2D solution landscape to heuristically explain the emergence of these $z$-variant 3D LdG saddle points. In fact, from H to B-W-B, the 2D H saddle points on the top and bottom surfaces relax to two different BD saddle points. From B-W-B to D-W-D, the 2D BD states on the top and bottom surfaces relax to two different D states; from D-W-D to D-B-D, the 2D WORS state on $z = 0$ relaxes to the BD state. At the base of the solution landscape, the D-B-D state stabilizes to the $z$-invariant D state, following the unstable eigenvector of the BD state on $z = 0$.

    These numerical results show that 3D $z$-invariant solutions can be generalized from 2D solutions, but with different Morse indices because 3D solutions can often accommodate unstable $z$-variant eigenvectors, and the $z$-variant LdG critical points usually accommodate two lower-index 2D solutions on the top and bottom surfaces accompanied by a higher-index 2D saddle point on $z = 0$, reminiscent of a pathway between two distinct 2D LdG critical points on the 2D solution landscape. This brings
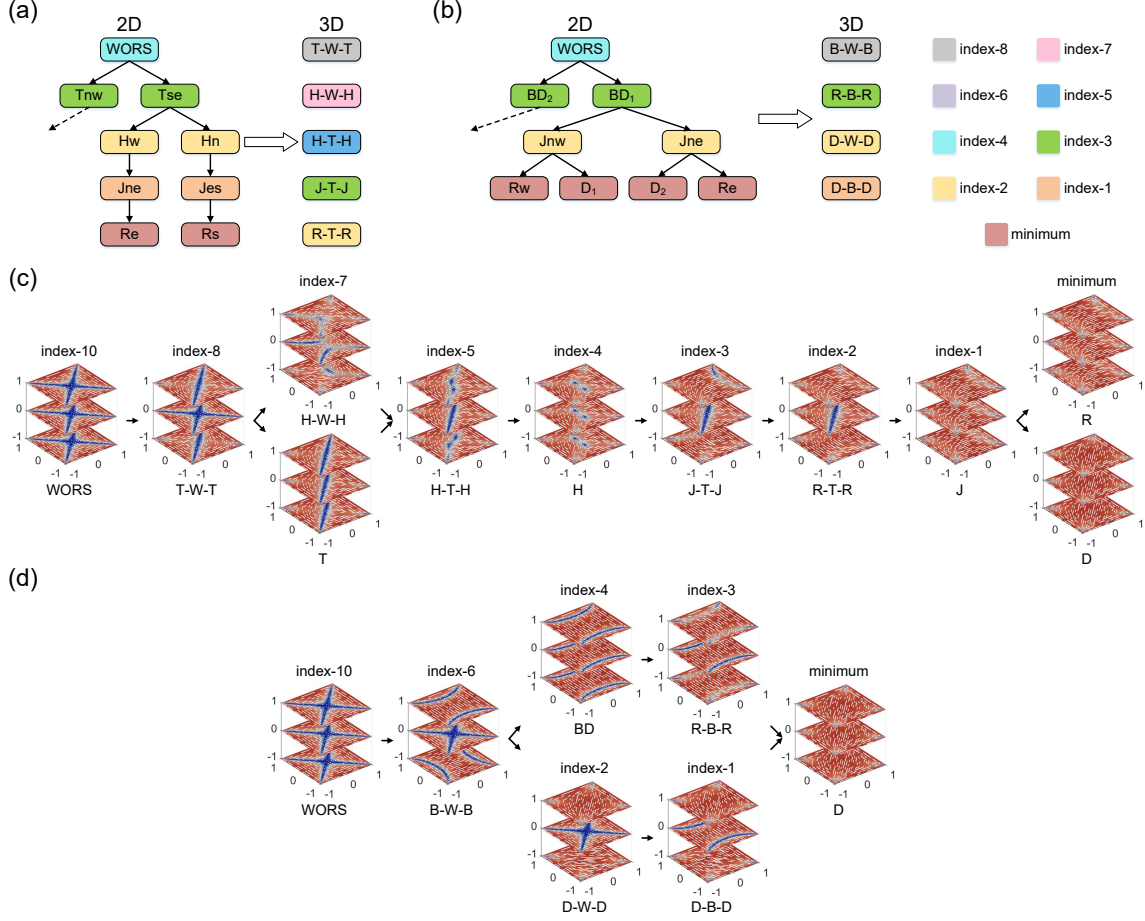
**Figure 6.** (a-b) are two pathway maps in the 2D solution landscape and the 3D solutions found by them at $\lambda^2 = 30$. (c-d) are the corresponding 3D configurations and their connections in (a-b). The colors of the node specify the Morse indices of saddle points. The subscripts (e=east, w=west, n=north, s=south) distinct rotationally equivalent solutions. The symmetrical part in the pathway maps is omitted by the dashed arrows.

us to a question - can we use pathways between distinct 2D LdG critical points as a database to construct 3D $z$-variant LdG critical points? The answer is affirmative and we use two 2D pathway maps, WORS→T→H→J→R and WORS→BD→J→D (R), to construct two branches of 3D solutions at $\lambda^2 = 30$ in Fig. 6.

As shown in Fig. 6(a), at $\lambda^2 = 30$, we have four 2D T states which are index-3, and the transition pathway between them passes through the index-4 WORS. We take this transition pathway as an initial guess and obtain a 3D $z$-variant LdG critical point, T-WORS-T, by using the SD. Similarly, we can obtain 3D $z$-variant LdG saddle points, H-W-T, H-T-H, J-T-J, and R-T-R from the following pathways on the 2D solution landscape: $H_n \rightarrow WORS \rightarrow H_s$, $H_n \rightarrow T_{se} \rightarrow H_w$, $J_{es} \rightarrow T_{se} \rightarrow J_{ne}$, and $R_s \rightarrow T_{se} \rightarrow R_e$, respectively. Combined with the $z$-invariant solutions, we construct a branch of 3D LdG critical points in Fig. 6(c) from Fig. 6(a). We observe that the 3D LdG critical points,

with a high-index 2D LdG saddle point on the top, bottom, and middle slices, usually have a high Morse index. As we progress from the parent state (WORS) of the 3D solution landscape, the indices of the 2D LdG critical points on the top and bottom typically decrease or the index of the 2D middle slice decreases. For example, the $z$-invariant WORS is an index-10 saddle point and relaxes to an index-8 T-W-T by relaxing the top and bottom surfaces to the 2D T profile (which is of lower 2D index than WORS). The T-W-T relaxes to an index-7 H-W-H critical point, by relaxing the T states to the H states, or relaxing the middle slice to T (which has lower index than WORS) results in a 3D $z$-invariant index-7 T state. The H-W-H relaxes the middle slice to T, or the $z$-invariant T state relaxes the top and bottom slices to the H state, so that both of these 3D LdG critical points relax to an index-5 H-T-H. The index-5 H-T-H further relaxes to index-4 $z$-invariant H state. The H-T-H state has two line defects running throughout the cuboid, that smoothly interpolate between the $+1/2$ planar point defect and $-1/2$ planar point defect on the top and bottom surfaces respectively, and this cannot be observed in 2D. A different lesson can be learnt from H$\rightarrow$ J-T-J and R-T-R $\rightarrow$ J; in some cases, we can decrease the index of a $z$-variant 3D LdG saddle point by increasing the index of the 2D critical point on the top, bottom or middle slices (but not all three simultaneously). For example, from the index-4 H to index-3 J-T-J, the Morse index of the middle slice increases, whilst the index of the top and bottom surfaces decreases. In fact, though the Morse index of a 2D T state is higher than 2D H state, J-T-J has a lower index than the $z$-invariant H critical point, since we cannot have a pathway between $J_{ne}$ and $J_{es}$ without crossing a T state, as is evident from the 2D solution landscape in Fig 6(a).

    Similarly, we use the 2D solution landscape in Fig. 6(b) to construct a branch of 3D LdG critical points in Fig. 6(d). From the index-10 WORS to the index-6 B-W-B, the top and bottom profiles change from the WORS to the BD state respectively. Following the unstable eigendirection of B-W-B, the WORS can move down and the B-W-B state relaxes to the 3D $z$-invariant BD state. From the index-4 $z$-invariant BD state to the index-3 R-B-R, the top and bottom profiles relax the BD to the R state. The index-2 D-W-D saddle point cannot be found by the downward search from BD and R-B-R, while it can be found from B-W-B, since the BD states on the top and bottom surfaces can easily relax to the D states. However, not all pathways on 2D solution landscapes lead to 3D LdG critical points i.e. we cannot construct the $z$-variant J-BD-J state from the 2D pathway $J_{nw} \rightarrow BD_1 \rightarrow J_{ne}$ at $\lambda^2 = 30$ due to the limit of the domain size, whereas we can find it for $\lambda^2 \geqslant 40$. This raises the fundamentally interesting question of whether we can provide algorithmic recipes for using pathways on 2D solution landscapes for systematically constructing 3D LdG critical points, in the $\lambda^2 \rightarrow \infty$ limit.

### 4.3. The transition pathways

The transition state is the index-1 saddle point and plays a key role in determining the energy barrier of such a transition pathway [41, 42, 43]. In this section, we compare two
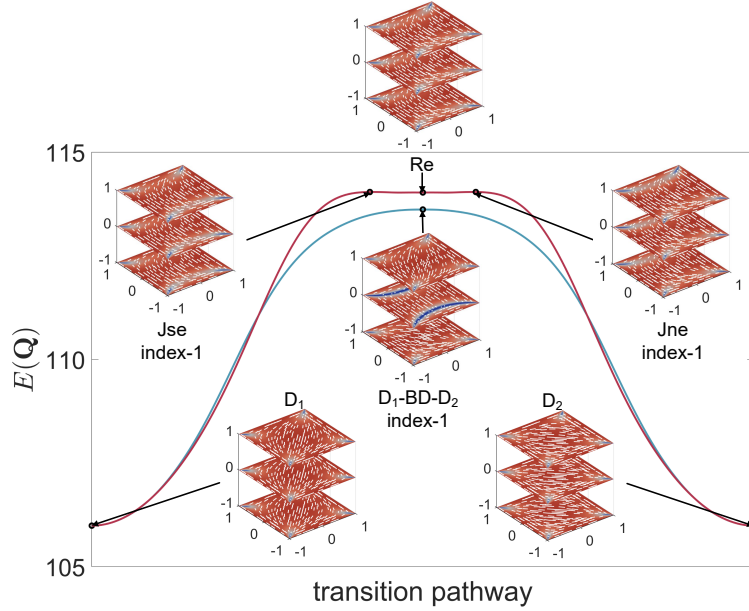
**Figure 7.** Transition pathways between two dual D states, $D_1$ and $D_2$, on a cube at $\lambda^2 = 30$, $h = 1$. The vertical axis is the LdG energy (4), and the horizontal axis describes the transition pathway.

different pathways between the $z$-invariant stable $D_1$ and $D_2$ states; the first pathway proceeds via $z$-invariant critical points and is identical to a pathway in the 2D solution landscape and the second pathway proceeds via a $z$-variant 3D LdG saddle point inaccessible in 2D studies. In the 2D case, $D_1$ and $D_2$ correspond to diagonal states with the director along a square diagonal; there are two diagonal states due to two orthogonal square diagonals. The $D_1$ and $D_2$ states cannot be connected by a single transition state in 2D for large domain size [17, 44]. The switching between $D_1$ and $D_2$ must go through a two-stage transition that involves the metastable R state and two energy barriers brought on by the transition states - $J_{se}$ and $J_{ne}$. In fact, the pathway sequence $D_1 \rightarrow J_{se} \rightarrow R_e \rightarrow J_{ne} \rightarrow D_2$ also exists in 3D and is a candidate for the switching pathway between the $z$-invariant $D_1$ and $D_2$ states on a cuboid (Fig. 7). However, in 3D, we can directly switch between the two dual D states by passing through the $z$-variant index-1 D-B-D saddle point, because the system can break the 2D restriction. We believe the second pathway is more likely to occur in practice than the first one, since it has a lower energy barrier and follows a single transition state (D-BD-D), without the risk of being trapped into metastable states such as the rotated states.

From our numerical results, we speculate that there will typically be an energetically favourite one-stage transition pathway between dual global minima, for 3D wells with polygonal cross-sections, where the transition state is a $z$-variant 3D LdG transition state. Such $z$-variant transition states are inaccessible in 2D scenarios. For instance, in a hexagon [19], the transition pathway between two dual stable Para states follows

a two-stage transition, with the risk of being trapped in a metastable state. If we generalize our work to 3D wells with a hexagonal cross-section, we will have $z$-variant 3D LdG critical points which could be exploited to generate new transition pathways between the dual globally stable Para states.

### 4.4. The effects of $\lambda^2$ and $h$ on the 3D Solution Landscape

In this section, we make some preliminary observations about the effects of $\lambda^2$ and $h$ on the NLC solution landscape. These observations are far from complete, but do set the scene for challenging analytic and numerical studies.

Our main observations can be summarized as follows. As $\lambda^2$ and $h$ increase, the solution landscape becomes increasingly complicated with a large number of $z$-variant LdG saddle points. In fact, as $h$ increases, the index of $z$-variant LdG saddle points decreases i.e. increasing $h$ stabilizes $z$-variant LdG critical points to some extent or at least suppresses some of their instabilities. Another notable observation is the emergence of *multiple-layer* solutions for large enough $\lambda^2$ and $h$. The multiple-layer solutions are effectively block solutions obtained by stacking $z$-variant LdG saddle points on top of each other. For example, (D-W-D)$^2$ is a LdG saddle point, compatible with the boundary conditions in (6), obtained by the superposition of two D-W-D saddle points.

We make these observations more precise by computing part of the bifurcation diagram, for solutions of (9) subject to (6), as a function of $\lambda^2$ with $h = 1$, in Fig. 8(a). We track the Morse indices of the solutions in Sec. 4.2, since a change in the Morse index signals the onset of a bifurcation [21]. The WORS is the unique LdG critical point for small enough $\lambda$, and has the highest Morse index in the bifurcation diagram; thus, WORS is typically used as the parent state to construct the 3D solution landscape. At $\lambda^2 = 7$, the WORS loses stability and bifurcates into a stable $z$-invariant D state. At $\lambda^2 = 10$, the index-1 WORS bifurcates into an index-2 $z$-invariant WORS and an index-1 $z$-invariant BD. At $\lambda^2 = 12$, an index-2 WORS bifurcates into an index-3 WORS, and an index-2 $z$-variant D-W-D which cannot be observed in the 2D case. More stable and unstable solutions can be numerically computed with large $\lambda^2$. It is noteworthy that the index-6 WORS bifurcates into an index-7 WORS, and an index-6 2-layer solution: (D-W-D)$^2$ which features two blocks of D-W-D, i.e., the chain D-W-D-W-D from the top to the bottom surface. This procedure could be repeated $n$ number of times in principle, to construct $n$-layer solutions for a positive integer $n$, and these multiple-layer solutions offer new optical and mechanical possibilities for designer materials technologies.

We also track part of the bifurcation diagram as a function of $h$ in Fig. 8(b), to study the effect of the cuboid height on the solution landscape, at $\lambda^2 = 19$. We only focus on the WORS and BD branches for simplicity. For $h = 0$, i.e., in the 2D case, the WORS is an index-4 saddle point and the BD is an index-2 saddle point. As $h$ increases, the WORS can accommodate $z$-variant unstable eigenvectors, and the index-4 WORS bifurcates into an index-5 WORS and an index-4 D-W-D at $h = 0.5$; the index-5 WORS bifurcates into an index-6 WORS and an index-5 B-W-B at $h = 0.7$.
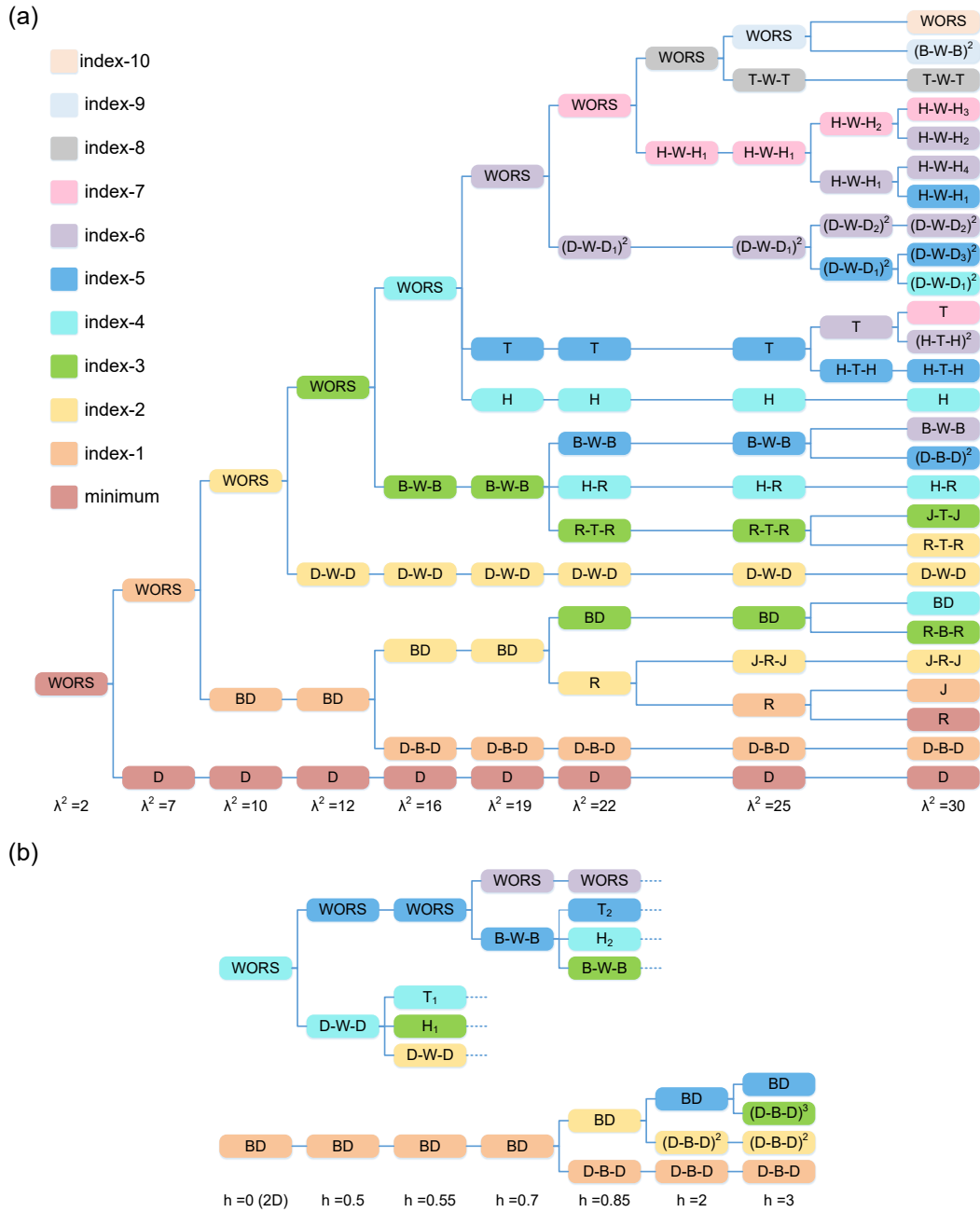
**Figure 8.** (a) Bifurcation diagram as a function of $\lambda^2$ at $h = 1$. (b) Bifurcation diagram as a function of $h$ at $\lambda^2 = 19$. Each small rectangle represents a solution as shown in Fig. 5 and Fig. 6 and the color represents the Morse index. The subscript is used to distinguish solutions with similar defect configurations and the superscript represents a solution accommodate multiple layers, e.g., $(D\text{-}B\text{-}D)^2$ has two layers of D-B-D. Each T-junction represents a pitchfork bifurcation. We omit some subsequent bifurcation by using the dashed line for a concise description.

At $h = 0.85$, the BD can accommodate $z$-variant unstable eigenvectors, and bifurcates into an index-2 BD and an index-1 D-B-D. As $h$ further increases, the $z$-invariant BD state can accommodate multiple $z$-variant unstable eigenvectors and bifurcates into an index-2 (D-B-D)$^2$ and an index-3 (D-B-D)$^3$ at $h = 2$ and $h = 3$, respectively.

As $h$ increases, the energetic penalty of distortions in the $z$-direction decreases which informally explains why we observe more $z$-variant LdG saddle points with decreasing Morse indices. In Fig. 2, we plot the smallest eigenvalue of the Hessian of the LdG energy at D-B-D as a function of $h$, which converges to zero as $h \to \infty$. As shown in Fig. 8(b), we also observe that the Morse index of D-W-D state decreases as $h$ increases. In the next subsection, we discuss the multiple-layer solutions in more detail. D-W-D and D-B-D have lower indices as $h$ increases.

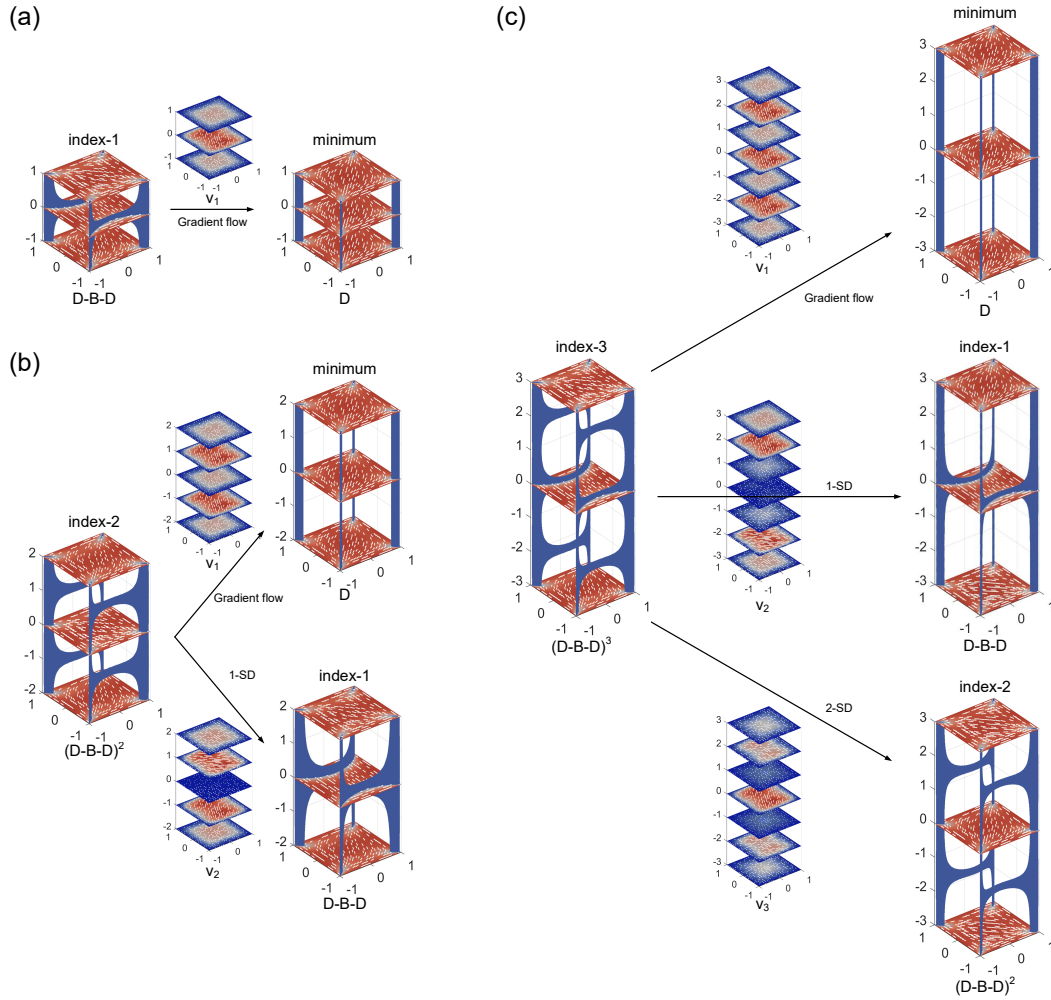### 4.5. Multiple–layer solutions (A1-B-A2-B-A1)



**Figure 9.** The D-B-D type solutions and the downward search along their unstable eigenvectors with (a) one layer (b) two layers and (c) three layers at $\lambda^2 = 30$.

In this section, we study the relationship between the Morse indices of multiple-

layer solutions and the number of layers, some of which has been touched on in Sec. 4.4. It is intuitive to expect that multiple-layers solutions, with more layers, have a higher Morse index, and we use the $D_2$-B-$D_1$ saddle point (labelled as D-B-D), to illustrate this point in Fig. 9. The one layer, D-B-D saddle point, is an index-1 saddle point. Following the disturbance along $\mathbf{v}_1$, the BD profile on the middle slice relaxes to the $D_1$ state, that is, the BD slice moves up, and the D-B-D saddle point relaxes to the $z$-invariant $D_1$ state, by following gradient flow dynamics (recall that there are two diagonal states, $D_1$ and $D_2$, corresponding to the two square diagonals of $\Omega$). The eigendirection, $\mathbf{v}_1$, is an unstable eigendirection, since the $z$-invariant D state is a stable state and has a lower energy than the D-B-D saddle point. The two-layer saddle point, $(D\text{-}B\text{-}D)^2$ $(D_1\text{-}B\text{-}D_2\text{-}B\text{-}D_1)$ is an index-2 saddle point with two unstable eigendirections, $\mathbf{v}_1$ and $\mathbf{v}_2$. Following the disturbance along $\mathbf{v}_1$, both of the BD states relax to $D_1$, and $(D\text{-}B\text{-}D)^2$ relaxes to the $z$-invariant $D_1$ state. Following the disturbance along $\mathbf{v}_2$, the top BD state relaxes to the $D_2$ state and given the natural boundary conditions, the $D_1$ state at the top also switches to the $D_2$ state, while the second BD state relaxes to the $D_1$ state. Hence, $(D\text{-}B\text{-}D)^2$ relaxes to the D-B-D saddle point, by following the 1-SD. Since the D-B-D saddle point has a lower elastic energy than the $(D\text{-}B\text{-}D)^2$ saddle point, and the $z$-invariant D state is a LdG energy minimizer, $\mathbf{v}_1$ and $\mathbf{v}_2$ are unstable eigendirections and the corresponding eigenvalues are ordered as $|\lambda_1| > |\lambda_2|$ and $0 > \lambda_2 > \lambda_1$. Consider the three-layer solution $D_2\text{-}B\text{-}D_1\text{-}B\text{-}D_2\text{-}B\text{-}D_1$, labelled by $(D\text{-}B\text{-}D)^3$ which is an index-3 saddle point, with three unstable eigendirections, $\mathbf{v}_1$, $\mathbf{v}_2$, and $\mathbf{v}_3$. Following the disturbance with $\mathbf{v}_1$, the three BD states relax to $D_1$, and the $(D\text{-}B\text{-}D)^3$ saddle point relaxes to the $z$-invariant $D_1$ state. Following the disturbance with $\mathbf{v}_2$, the bottom BD relaxes to $D_2$ state and the top BD relaxes to $D_1$ state, while the second BD state is almost unchanged. Consequently, the top block relaxes to $D_1$ and the bottom block relaxes to $D_2$, and the $(D\text{-}B\text{-}D)^3$ saddle point relaxes to the one-layer saddle point denoted by D-B-D. Following the disturbance with $\mathbf{v}_3$, the three BD cross-sections move downwards, and the bottom BD state relaxes to the $D_2$ state, and thus, the $(D\text{-}B\text{-}D)^3$ saddle point relaxes to the two-layer saddle point, $(D\text{-}B\text{-}D)^2$ $(D_2\text{-}B\text{-}D_1\text{-}B\text{-}D_2)$. Since $E(D)$ (the energy of the D state)$< E(D-B-D) < E((D-B-D)^2) < E((D-B-D)^3)$, $\mathbf{v}_i, i = 1, 2, 3$ are unstable eigendirections, and the corresponding negative eigenvalues are ordered as follows: $|\lambda_1| > |\lambda_2| > |\lambda_3|$.

Based on these numerical findings, our conjecture is that the multiple-layer solution, $(D\text{-}B\text{-}D)^n$ is an index-$n$ saddle point with unstable eigendirections $\mathbf{v}_1, \cdots, \mathbf{v}_n$. With the disturbance of $\mathbf{v}_i, 1 \leqslant i \leqslant n$, the $(D\text{-}B\text{-}D)^n$ relaxes to $(D\text{-}B\text{-}D)^{(i-1)}$ saddle point, by following the $(i-1)$-SD. If $n$ is even, then we have the same diagonal state ($D_1$ or $D_2$) at the top and bottom; if $n$ is odd, we necessarily have different diagonal states on the top and bottom. The energy of $(D\text{-}B\text{-}D)^{(i-1)}$ is lower than that of $(D\text{-}B\text{-}D)^n$, for all $1 \leqslant i \leqslant n$. It is an open question as to whether these numerical observations can be proven or generalized to other multiple-layer saddle points.
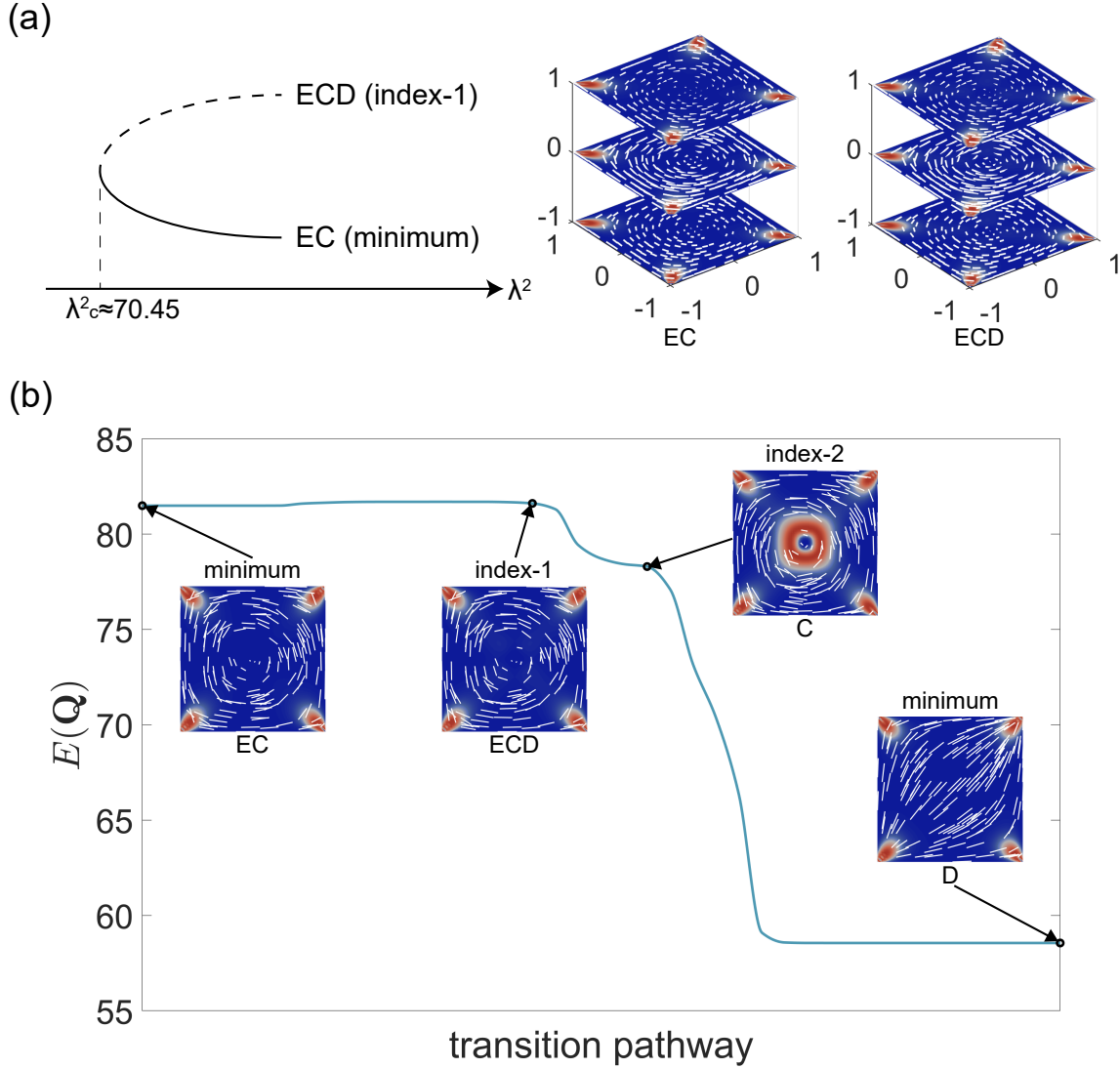
*4.6. Escaped solutions*



**Figure 10.** (a) The saddle-node bifurcation between EC and ECD, and the cross-section of the EC and ECD at $\lambda^2=74$. (b) The transition pathway beween EC and D in 2D case at $\lambda^2=74$. Color bar is the biaxiality parameter $\beta^2 = 1-6\mathrm{tr}(\mathbf{Q}^3)^2/(\mathrm{tr}(\mathbf{Q}^2))^3$ (see Sec. 2). The vertical axis is the 2D LdG energy and the horizontal axis describes the transition pathway.

Recall the five degrees of freedom of the LdG critical points denoted by $q_1, \ldots, q_5$ in (1). For the numerical results presented in the previous sections, we have $q_4 = q_5 = 0$, i.e. this physically means that $\mathbf{Q}$ has a fixed eigenvector in the $\mathbf{z}$ direction and the remaining two eigenvectors are in the $xy$-plane. In other words, the preceding numerical results only exploit 3 degrees of freedom - $q_1, q_2$ and $q_3$, with $q_3$ being largely constant. This raises the interesting question - do we have LdG critical points, with this choice of boundary conditions in (6) and natural boundary conditions on $z = \pm h$, that exploit the full five degrees of freedom? In [12], the authors demonstrate two escaped

*Hierarchies of Critical Points of a Landau-de Gennes Free Energy*        25

solutions with non-zero $q_4$ and $q_5$, and non-constant $q_3$, on a 2D square domain with an isotropic concentric square inclusion [12]. We build on the work in [12] and add Gaussian perturbation to the $z$-invariant C state (see Fig. 10(b) or [17]) to construct a suitable initial condition that converges to two escaped solutions in our framework. These escaped solutions exist for relatively large $\lambda^2$, and they are $z$-invariant stable states, labelled as escaped +1 center (EC+) and escaped -1 center (EC-), where $\pm 1$ indicates that the director rotates by $\pm\pi$ radians anticlockwise around the center. They have non-zero $q_4$ and $q_5$ profiles and are energetically degenerate, and hence, we only study the EC state with +1 center (Fig. 10(a)). Using the upward search, we can find an index-1 ECD from the stable index-0 EC state, for $\lambda^2 > 70.45$. In fact, the stable EC and index-1 ECD emerge from a saddle-node bifurcation at $\lambda^2 \approx 70.45$, without bifurcation connections with the WORS branch. As $\lambda^2$ increases, the EC state is always stable whilst the Morse index of the ECD increases, and bifurcates into multiple $z$-invariant and $z$-variant escaped solutions. We do not analyze this further in this paper, largely because the structure of this escaped branch is similar to the WORS branch in Sec. 4.

Since the EC and ECD LdG critical points are $z$-invariant, their cross-sections exist as critical points in 2D cases, for the same value of $\lambda^2$. The 2D ECD critical point is an index-1 saddle point, while the 2D EC is a metastable state since it has higher energy than the D state at $\lambda^2 = 74$. We investigate the transition pathway between EC and D in the 2D case at $\lambda^2 = 74$ (Fig. 10(b)). The transition state is the index-1 ECD state, and the energy barrier ( $E(ECD) - E(EC)$) is low, so that the system can easily escape from the trap of the metastable EC state. It is noteworthy that the transition pathway passes through an index-2 C state, which is connected to the WORS and the C state has only three degrees of freedom. In other words, in order to transition from the EC state (which exploits five degrees of freedom) to the D state (which exploits three degrees of freedom, or two degrees of freedom if $q_3$ is constant as in (5)), the escaped directors are pulled back into the $xy$-plane, and the transition pathway goes from escaped branch to the WORS branch, and finally, reaches the D state.

## 5. Discussion and conclusion

We study critical points of a LdG free energy on a 3D cuboid with Dirichlet tangent boundary conditions on lateral surfaces and natural boundary condition on top and bottom surfaces, in terms of two geometry-dependent variables: the cuboid size $\lambda$, and the height $h$. First, we design a hybrid numerical scheme to discretize and accelerate the saddle dynamics. It is worth noting that our new numerical scheme can be directly generated to other domains (e.g. 3D wells with other polygonal cross-sections) and boundary conditions (e.g. weak tangential boundary condition).

Our notable findings include (i) $z$-variant LdG critical points that depend on the third dimension, (ii) new pathways between energy minimizers mediated by $z$-variant critical points which are inaccessible in 2D, (iii) multiple-layer LdG critical points and

*Hierarchies of Critical Points of a Landau-de Gennes Free Energy*   26

(iv) novel stable escaped solution branches. Essentially, the solution landscapes become increasingly complicated as $\lambda^2$ and $h$ increases. We find intimate connections between pathways on 2D solution landscapes (for 2D domains in a reduced LdG framework) and $z$-variant 3D LdG critical points. Whilst our work is not exhaustive, we can typically construct $z$-variant 3D LdG critical points by interpolating between two distinct 2D reduced LdG critical points, and the interpolation usually involves a third higher-index 2D critical point on the middle slice of the cuboid. Of course, not all pairs of 2D reduced LdG critical points are compatible; we typically need 2D dual critical points that are connected by a pathway on the 2D solution landscape, to construct the $z$-variant 3D counterpart. As $\lambda \to \infty$, we speculate that we could use the entire database of dual 2D critical points to construct $z$-variant 3D LdG critical points. We note that the 2D studies in [11, 12, 17] provide excellent initial conditions for the 3D solvers (with five degrees of freedom) in our paper, and hence, reduced studies have value in higher dimensions too.

There are numerous open questions stemming from this work, which could have far-reaching impact in mathematics and applications. For example, can we have 3D LdG critical points that interpolate between escaped solution and a non-escaped solution? Are there other disconnected LdG critical points on a 3D cuboid and if so, how to find them? Our working domain is a cuboid with a square cross-section, but these methods could be easily generalized to a 3D well with an arbitrary 2D cross-section e.g. rectangle, hexagons etc. In fact, on a rectangle, we lose the degeneracy between different critical points e.g. the dual BD states are not energetically degenerate on a rectangle and the 2D WORS branch divides into two unconnected branches [21]. Thus, some of the solutions in this paper, e.g., BD-WORS-BD will have a different structure for a 3D well with a rectangular cross-section. Finally, we could work with weak tangential anchoring on the lateral well surfaces, as opposed to Dirichlet conditions. In particular, the nematic director profile on the lateral surfaces is constrained to be one-dimensional by (6), which severely constrains the solution space. Weak boundary conditions allow for more freedom on the lateral surfaces, which naturally adds further possibilities for the corresponding solution landscapes. Finally, there is scope for rigorous asymptotic analysis in the $\lambda^2 \to \infty$ limit [14], and we expect close correspondence with some of the analytic results in [45] in this limit.

## Acknowledgements

*Hierarchies of Critical Points of a Landau-de Gennes Free Energy*      27

## References

[1] P. G. De Gennes and J. Prost. *The physics of liquid crystals*. Number 83. Oxford University Press, 1993.

[2] A. A. Sonin. Pierre-Gilles de Gennes and physics of liquid crystals. *Liquid Crystals Reviews*, 6(2):109–128, 2018.

[3] I. W. Stewart. *The static and dynamic continuum theory of liquid crystals: a mathematical introduction*. Crc Press, 2019.

[4] G. Duclos, R. Adkins, D. Banerjee, and et al. Topological structure and dynamics of three-dimensional active nematics. *Science*, 367(6482):1120–1124, 2020.

[5] G. Foffano, J. Lintuvuori, A. Tiribocchi, and D. Marenduzzo. The dynamics of colloidal intrusions in liquid crystals: A simulation perspective. *Liquid Crystals Reviews*, 2(1):1–27, 2014.

[6] D. S. Miller, X. Wang, and N. L. Abbott. Design of functional materials based on liquid crystalline droplets. *Chemistry of Materials*, 26(1):496–506, 2014.

[7] J. P. F. Lagerwall and G. Scalia. A new era for liquid crystal research: Applications of liquid crystals in soft matter nano-, bio- and microtechnology. *Current Applied Physics*, 12(6):1387–1412, 2012.

[8] M. Doi and S. F. Edwards. *The theory of polymer dynamics*, volume 73. Oxford University Press, 1988.

[9] Wei Wang, Lei Zhang, and Pingwen Zhang. Modelling and computation of liquid crystals. *Acta Numerica*, 30:765–851, 2021.

[10] G. Canevari, A. Majumdar, and A. Spicer. Order reconstruction for nematics on squares and hexagons: A Landau–de Gennes study. *SIAM Journal on Applied Mathematics*, 77(1):267–293, 2017.

[11] M. Robinson, C. Luo, P. E. Farrell, R. Erban, and A. Majumdar. From molecular to continuum modelling of bistable liquid crystal devices. *Liquid Crystals*, 44(14-15):2267–2284, 2017.

[12] Y. Wang, G. Canevari, and A. Majumdar. Order reconstruction for nematics on squares with isotropic inclusions: A Landau–De Gennes study. *SIAM Journal on Applied Mathematics*, 79(4):1314–1340, 2019.

[13] Y. Han, J. Harris, L. Zhang, and A. Majumdar. Elastic anisotropy of nematic liquid crystals in the two-dimensional landau-de gennes model. *arXiv preprint arXiv:2105.10253*, 2021.

[14] Y. Han, A. Majumdar, and L. Zhang. A reduced study for nematic equilibria on two-dimensional polygons. *SIAM Journal on Applied Mathematics*, 80(4):1678–1703, 2020.

[15] C. Tsakonas, A. Davidson, C. Brown, and N. J. Mottram. Multistable alignment states in nematic liquid crystal filled wells. *Applied physics letters*, 90(11):111913, 2007.

[16] S. Kralj and A. Majumdar. Order reconstruction patterns in nematic liquid crystal wells. *Proceedings of the Royal Society A: Mathematical, Physical and Engineering Sciences*, 470(2169):20140276, 2014.

[17] J. Yin, Y. Wang, J. Z. Chen, P. Zhang, and L. Zhang. Construction of a pathway map on a complicated energy landscape. *Physical Review Letters*, 124(9):090601, 2020.

[18] Y. Hu, Y. Qu, and P. Zhang. On the disclination lines of nematic liquid crystals. *Communications in Computational Physics*, 19(2):354–379, 2016.

[19] Y. Han, J. Yin, P. Zhang, A. Majumdar, and L. Zhang. Solution landscapes of nematic liquid crystals confined on a hexagon. *Nonlinearity*, 34(4):2048, 2021.

[20] L. Fang, A. Majumdar, and L. Zhang. Surface, size and topological effects for some nematic equilibria on rectangular domains. *Mathematics and Mechanics of Solids*, 25(5):1101–1123, 2020.

[21] B. Shi, Y. Han, and L. Zhang. Nematic liquid crystals in a rectangular confinement: solution landscape and bifurcation. *arXiv preprint arXiv:2109.10318*, 2021.

[22] B. S. Gallardo, V. K. Gupta, F. D. Eagerton, and et al. Electrochemical principles for active control of liquids on submillimeter scales. *Science*, 283(5398):57–60, 1999.

[23] C. Long, X. Tang, R. L. Selinger, and J. V. Selinger. Geometry and mechanics of disclination lines in 3D nematic liquid crystals. *Soft Matter*, 17(8):2265–2278, 2021.

[24] G. Canevari, J. Harris, A. Majumdar, and Y. Wang. The well order reconstruction solution for three-dimensional wells, in the Landau–de Gennes theory. *International Journal of Nonlinear Mechanics*, 119:103342, 2020.

[25] Y. Han, Y. Hu, P. Zhang, and L. Zhang. Transition pathways between defect patterns in confined nematic liquid crystals. *Journal of Computational Physics*, 396:1–11, 2019.

[26] T. Machon and G. P. Alexander. Knotted defects in nematic liquid crystals. *Physical Review Letters*, 113(2):027801, 2014.

[27] N. J. Mottram and C. J. Newton. Introduction to Q-tensor theory. *arXiv preprint arXiv:1409.3542*, 2014.

[28] P. J. Wojtowicz, P. Sheng, and E. B. Priestley. *Introduction to liquid crystals.* Springer, 1975.

[29] A. Majumdar. Equilibrium order parameters of nematic liquid crystals in the Landau–de Gennes theory. *European Journal of Applied Mathematics*, 21(2):181–203, 2010.

[30] A. Majumdar and Z. Arghir. Landau–de gennes theory of nematic liquid crystals: the oseen–frank limit and beyond. *Archive for rational mechanics and analysis*, 196(1):227–280, 2010.

[31] C. Luo, A. Majumdar, and R. Erban. Multistability in planar liquid crystal wells. *Physical Review E*, 85(6):061702, 2012.

[32] W. E., W. Ren, and E. Vanden-Eijnden. String method for the study of rare events. *Physical Review B*, 66(5):052301, 2002.

[33] W. E., W. Ren, and E. Vanden-Eijnden. Simplified and improved string method for computing the minimum energy paths in barrier-crossing events. *Journal of Chemical Physics*, 126(16):164103, 2007.

[34] J. Yin, L. Zhang, and P. Zhang. High-index optimization-based shrinking dimer method for finding high-index saddle points. *SIAM Journal on Scientific Computing*, 41(6):A3576–A3595, 2019.

[35] J. Yin, Z. Huang, and L. Zhang. Constrained high-index saddle dynamics for the solution landscape with equality constraints. *arXiv preprint arXiv:2011.13173*, 2020.

[36] L. Zhang, P. Zhang, and X. Zheng. Optimal-order error estimates for euler discretization of high-index saddle dynamics. *arXiv preprint arXiv:2111.05156*, 2021.

[37] J. Yin, L. Zhang, and P. Zhang. Solution landscape of the onsager model identifies non-axisymmetric critical points. *Physica D*, 430:133081, 2022.

[38] A. V. Knyazev. Toward the optimal preconditioned eigensolver: Locally optimal block preconditioned conjugate gradient method. *SIAM Journal on Scientific Computing*, 23:517–541, 2001.

[39] J. Barzilai and J. M. Borwein. Two-point step size gradient methods. *IMA Journal of Numerical Analysis*, 8(1):141–148, 1988.

[40] J. Yin, B. Yu, and L. Zhang. Searching the solution landscape by generalized high-index saddle dynamics. *Sci. China Math.*, 64(8):1801–1816, 2021.

[41] L. Zhang, L. Q. Chen, and Q. Du. Morphology of critical nuclei in solid-state phase transformations. *Physical review letters*, 98(26):265703, 2007.

[42] Y. Zhang, Y. Li, L. Zhang, and S. Sun. Construction of a minimum energy path for the vt flash model by the string method coupled with the exponential time differencing scheme. *Communications in Computational Physics*, 30(5):1529–1544, 2021.

[43] J. Yin, K. Jiang, A. C. Shi, P. Zhang, and L. Zhang. Transition pathways connecting crystals and quasicrystals. *Proceedings of the National Academy of Sciences*, 118(49), 2021.

[44] H. Kusumaatmaja and A. Majumdar. Free energy pathways of a multistable liquid crystal device. *Soft Matter*, 11(24):4809–4817, 2015.

[45] A. Majumdar, J. M. Robbins, and M. Zyskin. Energies of $s^2$-valued harmonic maps on polyhedra with tangent boundary conditions. *arXiv preprint arXiv:math-ph/0606024*, 2006.